NASA/CR—2004-213379

Detached-Eddy Simulations of Separated Flow Around Wings With Ice Accretions: Year One Report

David Thompson and Prasad Mogili
Mississippi State University, Mississippi State University, Mississippi

November 2004

The NASA STI Program Office . . . in Profile

Since its founding, NASA has been dedicated to the advancement of aeronautics and space science. The NASA Scientific and Technical Information (STI) Program Office plays a key part in helping NASA maintain this important role.

The NASA STI Program Office is operated by Langley Research Center, the Lead Center for NASA's scientific and technical information. The NASA STI Program Office provides access to the NASA STI Database, the largest collection of aeronautical and space science STI in the world. The Program Office is also NASA's institutional mechanism for disseminating the results of its research and development activities. These results are published by NASA in the NASA STI Report Series, which includes the following report types:

- TECHNICAL PUBLICATION. Reports of completed research or a major significant phase of research that present the results of NASA programs and include extensive data or theoretical analysis. Includes compilations of significant scientific and technical data and information deemed to be of continuing reference value. NASA's counterpart of peer-reviewed formal professional papers but has less stringent limitations on manuscript length and extent of graphic presentations.

- TECHNICAL MEMORANDUM. Scientific and technical findings that are preliminary or of specialized interest, e.g., quick release reports, working papers, and bibliographies that contain minimal annotation. Does not contain extensive analysis.

- CONTRACTOR REPORT. Scientific and technical findings by NASA-sponsored contractors and grantees.

- CONFERENCE PUBLICATION. Collected papers from scientific and technical conferences, symposia, seminars, or other meetings sponsored or cosponsored by NASA.

- SPECIAL PUBLICATION. Scientific, technical, or historical information from NASA programs, projects, and missions, often concerned with subjects having substantial public interest.

- TECHNICAL TRANSLATION. English-language translations of foreign scientific and technical material pertinent to NASA's mission.

Specialized services that complement the STI Program Office's diverse offerings include creating custom thesauri, building customized databases, organizing and publishing research results . . . even providing videos.

For more information about the NASA STI Program Office, see the following:

- Access the NASA STI Program Home Page at ***http://www.sti.nasa.gov***

- E-mail your question via the Internet to help@sti.nasa.gov

- Fax your question to the NASA Access Help Desk at 301–621–0134

- Telephone the NASA Access Help Desk at 301–621–0390

- Write to:
  NASA Access Help Desk
  NASA Center for AeroSpace Information
  7121 Standard Drive
  Hanover, MD 21076

NASA/CR—2004-213379

Detached-Eddy Simulations of Separated Flow Around Wings With Ice Accretions: Year One Report

David Thompson and Prasad Mogili
Mississippi State University, Mississippi State University, Mississippi

Prepared under Grant NAG3–2892

National Aeronautics and
Space Administration

Glenn Research Center

November 2004

Available from

NASA Center for Aerospace Information
7121 Standard Drive
Hanover, MD 21076

National Technical Information Service
5285 Port Royal Road
Springfield, VA 22100

Available electronically at http://gltrs.grc.nasa.gov

Contents

1. Introduction **1**

2. Detached Eddy Simulation **3**

3. Numerical Considerations **4**
3.1 Problem statement 4
3.2 Geometry modeling 4
3.3 Mesh Generation: Estimated DES zones for iced wing 4
3.4 Selection of mesh spacing in focus region 5
3.5 Selection of time-step size 6
3.6 Unstructured mesh generation using SolidMesh and VGridns/GridTool 6
3.7 Flow solution 7

4. Results **11**
4.1 Experimental details 11
4.2 RANS results 16
4.3 DES results 31
4.3.1 Two-dimensional DES results 31
4.3.2 Three-dimensional DES results: 4° angle of attack, Δt=0.15ms, baseline mesh . . . 35
4.3.3 Three-dimensional DES results: 6° angle of attack, Δt=0.15ms, baseline mesh . . . 40
4.3.4 Three-dimensional DES results: 6° angle of attack, Δt=0.075ms, baseline mesh . . 46
4.3.5 Three-dimensional DES results: 6° angle of attack, Δt=0.075ms, refined mesh . . . 52
4.3.6 Mesh refinement and time step refinement comparisons 58

5. Assessment of Existing Capabilities and Recommendations **65**
5.1 Tool assessment 65
5.2 Recommendations 65

6. Summary **66**

List of Figures

1 Estimated DES zones for GLC305 airfoil section with two-dimensional 944-ice shape (extruded wing) . . . 5
2 "Sources" used by GridTool/VGridns to generate mesh . . . 7
3 Mesh in cutting planes for extruded GLC305/944-ice shape (extruded wing) . . . 8
4 Two-dimensional mesh for GLC305/944-ice shape . . . 9
5 Comparison of experimental lift and drag coefficients for extruded GLC305 airfoil section: with and without 944-ice accretion [17] . . . 13
6 Comparison of experimental pressure coefficients for extruded GLC305 airfoil section: with and without 944-ice accretion [17] . . . 14
7 Experimental u-velocity contours for the extruded wing at angles of attack of $0°$, $4°$ and $6°$ [18] . . . 15
8 Convergence of RANS solution for extruded wing (baseline DES mesh at a $6°$ angle of attack) 18
9 Comparison of predicted (RANS) force coefficients and experimental data for the extruded wing (coarse RANS mesh, baseline DES mesh, and refined DES mesh) . . . 19
10 Comparison of predicted (RANS) midspan pressure coefficients and experimental data for the extruded wing at $0°$ angle of attack . . . 20
11 Comparison of predicted (RANS) midspan pressure coefficients and experimental data for the extruded wing at $2°$ angle of attack . . . 21
12 Comparison of predicted (RANS) midspan pressure coefficients and experimental data for the extruded wing at $4°$ angle of attack . . . 22
13 Comparison of predicted (RANS) midspan pressure coefficients and experimental data for the extruded wing at $6°$ angle of attack . . . 23
14 Comparison of predicted (RANS) midspan u-velocity contours and experimental data for the extruded wing at $0°$ angle of attack . . . 24
15 Comparison of predicted (RANS) midspan u-velocity contours and experimental data for the extruded wing at $4°$ angle of attack . . . 25
16 Comparison of predicted (RANS) midspan u-velocity contours and experimental data for the extruded wing at $6°$ angle of attack . . . 26
17 Comparison of predicted (RANS) upper surface separation (red) and attachment (blue) locations for the extruded wing at $0°$ angle of attack . . . 27
18 Comparison of predicted (RANS) upper surface separation (red) and attachment (blue) locations for the extruded wing at $2°$ angle of attack . . . 28
19 Comparison of predicted (RANS) upper surface separation (red) and attachment (blue) locations for the extruded wing at $4°$ angle of attack . . . 29
20 Comparison of predicted (RANS) upper surface separation (red) and attachment (blue) locations for the extruded wing at $6°$ angle of attack . . . 30
21 Comparison of predicted time-averaged u-velocity contours and experimental data for the extruded wing (two-dimensional baseline DES mesh, and two-dimensional refined DES mesh at $4°$ angle of attack with Δt=0.075ms) . . . 32
22 Comparison of predicted time-averaged u-velocity contours and experimental data for the extruded wing (two-dimensional baseline DES mesh, and two-dimensional refined DES mesh at $6°$ angle of attack with Δt=0.075ms) . . . 33
23 Instantaneous vorticity plots for two-dimensional baseline mesh at $6°$ angle of attack with Δt=0.15ms . . . 34
24 Comparison of predicted midspan wing pressure coefficients and experimental data for the extruded wing (baseline mesh at $4°$ angle of attack with Δt=0.15ms) . . . 36

25 Comparison of predicted midspan u-velocity contours and experimental data for the extruded wing (baseline mesh at 4° angle of attack with Δt=0.15ms) 37
26 Comparison of predicted separation (red) and attachment (blue) locations for the extruded wing (baseline mesh at 4° angle of attack with Δt=0.15ms) 38
27 Comparison of the RMS of the fluctuations in the u-velocity component for the extruded wing (baseline mesh at 4° angle of attack with Δt=0.15ms) 39
28 Comparison of predicted midspan wing pressure coefficients and experimental data for the extruded wing (baseline mesh at 6° angle of attack with Δt=0.15ms) 41
29 Comparison of predicted midspan u-velocity contours and experimental data for the extruded wing (baseline mesh at 6° angle of attack with Δt=0.15ms) 42
30 Comparison of predicted separation (red) and attachment (blue) locations for the extruded wing (baseline mesh at 6° angle of attack with Δt=0.15ms) 43
31 Comparison of the RMS of the fluctuations in the u-velocity component for the extruded wing (baseline mesh at 6° angle of attack with Δt=0.15ms) 44
32 Isovorticity contours ($300s^{-1}$) colored by pressure for the DES baseline mesh at 6° angle of attack with Δt=0.15ms 45
33 Comparison of predicted midspan wing pressure coefficients and experimental data for the extruded wing (baseline mesh at 6° angle of attack with Δt=0.075ms) 47
34 Comparison of predicted midspan u-velocity contours and experimental data for the extruded wing (baseline mesh at 6° angle of attack with Δt=0.075ms) 48
35 Comparison of predicted separation (red) and attachment (blue) locations for the extruded wing (baseline mesh at 6° angle of attack with Δt=0.075ms) 49
36 Comparison of the RMS of the fluctuations in the u-velocity component for the extruded wing (baseline mesh at 6° angle of attack with Δt=0.075ms) 50
37 Isovorticity contours ($300s^{-1}$) colored by pressure for the DES baseline mesh at 6° angle of attack with Δt=0.075ms 51
38 Comparison of predicted midspan wing pressure coefficients and experimental data for the extruded wing (refined mesh at 6° angle of attack with Δt=0.075ms) 53
39 Comparison of predicted midspan u-velocity contours and experimental data for the extruded wing (refined mesh at 6° angle of attack with Δt=0.075ms) 54
40 Comparison of predicted separation (red) and attachment (blue) locations for the extruded wing (refined mesh at 6° angle of attack with Δt=0.075ms) 55
41 Comparison of the RMS of the fluctuations in the u-velocity component for the extruded wing (refined mesh at 6° angle of attack with Δt=0.075ms) 56
42 Isovorticity contours ($300s^{-1}$) colored by pressure at 6° angle of attack with Δt=0.075ms . 57
43 Comparison of predicted wing lift and drag coefficients and experimental data for the extruded wing (coarse RANS mesh, baseline DES mesh and refined DES mesh) 60
44 Comparison of predicted midspan wing pressure coefficients and experimental data for the extruded wing (coarse RANS mesh, baseline DES mesh and refined DES mesh at 6° angle of attack) 61
45 Lift history for refined mesh with Δt=0.075ms 62
46 Comparison of power spectral density plots for baseline mesh and refined mesh at 6° angle of attack, with Δt=0.075ms 63
47 Comparison of power spectral density plots for baseline mesh at 6° angle of attack with, Δt=0.15ms and Δt=0.075ms 64

List of Tables

1 Statistics for the meshes employed in this effort 10
2 Two-dimensional DES time-averaged lift and drag coefficients on the baseline mesh, for different time steps at 6° angle of attack 31
3 Comparison of predicted lift and drag coefficients and experimental data for the extruded wing (baseline mesh at 4° angle of attack with Δt=0.15ms) 35
4 Comparison of predicted lift and drag coefficients and experimental data for the extruded wing (baseline mesh at 6° angle of attack with Δt=0.15ms) 41
5 Comparison of predicted lift and drag coefficients and experimental data for the extruded wing (baseline mesh at 6° angle of attack with Δt=0.075ms) 46
6 Comparison of predicted lift and drag coefficients and experimental data for the extruded wing (refined mesh at 6° angle of attack with Δt=0.075ms) 52
7 Comparison of lift and drag coefficients for all three-dimensional RANS and DES results (coarse RANS mesh, baseline DES mesh and refined DES mesh) 59

Nomenclature

$\hat{S}$	Local strain rate
$\widetilde{d}$	Modified wall distance (used in DES model)
$\widetilde{\nu}$	Working variable in Spalart-Allmaras turbulence model
α	Angle of attack in degrees
Δ	Local mesh spacing
Δ_0	Mesh spacing in focus region
Δt	Estimated time step size
θ	AVUS time integration parameter
λ	Wavelength of smallest resolved eddy
c	Airfoil chord length
C_D	Drag coefficient
C_{DES}	Constant employed in DES model (usually taken to be 0.65)
C_L	Lift coefficient
C_P	Pressure coefficient
d	Distance to nearest wall
M	Mach number
Re	Reynolds number based on the chord
t	Solution time
$t^* = \frac{tU_\infty}{c}$	Non-dimensional time
U_0	Maximum flow velocity in focus region
	of unity in the focus region
U_∞	Freestream velocity
y^+	Distance to the first point off the wall

1. Introduction

It is well known and appreciated that the accretion of ice on lifting surfaces can significantly degrade the performance and handling characteristics of affected aircraft [1]. Less well understood, however, are the details of the complex flow fields associated with these configurations. These flow fields may exhibit extensive regions of unsteady separated flow depending on the ice shape. Typically, ice accretions on straight wings are categorized as "rime," "horn," or "spanwise ridge," which are more or less two-dimensional in nature, or "roughness," which is the most three-dimensional of the shapes [1]. The flow field for a horn ice accretion, which is the subject of this effort, is dominated by a separation bubble downstream of the horn. The flow separates because it is unable to recover the necessary pressure in the boundary layer after it expands around the horn. The ensuing free shear layer rolls up to form vortices that are convected downstream. The development of this unsteady flow field is critical to the resulting flow near maximum lift. The separation bubble has a large global effect and is similar to the long bubble defined by Tani [2].

Many researchers have turned to computational fluid dynamics (CFD) simulations to investigate iced wing flow fields. Beginning with Potapczuk [3], numerous results from icing effects studies using the Reynolds averaged Navier-Stokes (RANS) equations have been reported in the literature. Chung, et al. [4], analyzed the flow around the ice contaminated wing surfaces of a turbo-prop aircraft. Their two- and three-dimensional analyses of a wing with a spanwise ridge accretion employed a steady RANS approach and were performed to provide insight into the aerodynamics that may have led to a loss of control of the aircraft. Reported discrepancies between the two- and three-dimensional results were attributed to a lack of grid resolution for the three-dimensional cases considered. Dunn and Loth [5] studied the effects of simulated-spanwise-ice shapes on the aerodynamic performance of two-dimensional wing sections using a RANS solver developed for unstructured meshes. A forward-facing quarter round was employed as the simulated ice shape. Additionally, they employed a solution adaptive mesh in which the mesh was refined in the separated shear layer. Their results showed that, even with adaptive mesh refinement, the pressure recovery was not correctly predicted. This discrepancy was attributed to the inability of the steady RANS simulation to model the experimentally observed unsteadiness that occurs in flow fields of this type. Pan, Loth, and Bragg [6] performed RANS simulations for flow about airfoils with ridge ice shapes and leading edge ice shapes and compared the results to experimental data. Favorable comparisons between predicted force data and experiments were obtained up to, but not including, the stall condition, which is dominated by unsteady flow.

Recently, researchers have begun employing unsteady simulations to investigate separated flow fields. Candidate approaches for computing such unsteady flow fields include unsteady RANS (URANS), direct numerical simulation (DNS), large-eddy simulation, (LES), and detached eddy simulation (DES). Spalart [7] contends that URANS is both "ambiguous and flawed" and that "its quantitative performance can be quite poor." DNS, while attractive from the standpoint that no modeling is required, and LES are currently impractical for realistic configurations due to their computational expense. DES, however, appears to have the potential to represent a viable near-term approach. DES is a hybrid RANS/LES approach in which a RANS turbulence model is employed in attached thin shear layers and an LES-type model is employed in regions away from the wall. This approach exploits the ability of RANS simulations to efficiently model high Reynolds number attached boundary layer flows and the ability of LES to model geometry dependent, unsteady three-dimensional flows [8]. DES has been employed in numerous simulations of complex flow fields [9–11]. DES has also been applied to the icing effects problem. Kumar and Loth [12] employed a DES technique to predict the unsteady flow around an NLF0414 airfoil section with a synthetic ice shape located on the upper surface at 3.4% chord. They also reported on computations for a rectangular three-dimensional wing using the same section. Their three-dimensional results showed some improvement relative to the steady RANS computations. Pan and Loth [13] performed a DES for an NACA23012 airfoil with forward-facing quarter-round simulated ice accretion. Again, some improvement between the predicted results and

experimental data was reported.

We previously reported results from steady RANS simulations for a horn ice shape/wing configuration [14, 15]. The basic ice shape considered was a 22.5-minute glaze ice accretion on a GLC305 airfoil, which is denoted as the two-dimensional 944-ice shape [16]. The airfoil section/ice shape was extruded to form a rectangular planform wing with an aspect ratio of unity. The flow fields associated with this configuration have been studied experimentally and the results reported in [17, 18]. These data include force measurements and pressure measurements as well as mean velocity measurements and RMS fluctuations of the streamwise and transverse velocity components obtained using a split-hot-film probe. The model was mounted between the tunnel walls, so no tip effects were considered. We compared steady RANS results computed using the noncommercial version of the Cobalt_{60} code [19] (now called AVUS) and the Spalart-Allmaras turbulence model [20] with the experimental data. In general, the steady RANS computations underpredicted both the lift and drag as the angle of attack was increased. Additionally, the extent of the separated region was overpredicted even at lower angles of attack. As noted above for other RANS computations, the pressure recovery was not in agreement with the experimental data. In a related effort, Chi, et al. [21] reported on the results of a series of two-dimensional steady RANS simulations for the GLC305/944-ice shape, as well as a rime ice shape, using a variety of turbulence models. The two-dimensional results for the 944-ice shape were qualitatively very similar to those reported in Ref. [14, 15] regardless of the turbulence model employed. Additionally, relatively fine meshes were employed to discretize the computational domain. Therefore, we believe the discrepancies reported in Ref. [21] were not related to mesh effects.

In this report, we focus on activities associated with the first year of an effort to investigate the capability of existing flow simulation methodologies to predict the separated, highly unsteady flow fields associated with wings with significant horn-ice accretions. Here, we present the results of steady RANS computations and unsteady DES computations performed for the rectangular planform, extruded GLC305/944-ice shape wing. We first provide a brief discussion of the DES approach. We then provide a more concrete definition of the problem. Numerical considerations regarding how the mesh spacing and time step size are selected along with the mesh generation and solution procedures are discussed next. We present sample results from two-dimensional and three-dimensional computations. We then provide an assessment of the tools we employed and make a few recommendations regarding the roles of RANS and DES computations for icing effects studies. We conclude with a brief summary of the effort.

2. Detached Eddy Simulation

DES was originally formulated as a modification to the Spalart-Allmaras turbulence model [8, 20]. The basic idea is to employ a RANS-type turbulence model for thin, attached shear layers and an LES model in separated regions. This approach exploits the ability of RANS simulations to efficiently model attached boundary layer flows and the ability of LES to model unsteady, geometry-dependent, three-dimensional flow fields. RANS-type models perform well for attached flows and less well for separated flows, while LES models perform well for separated flows but are prohibitively expensive to employ for computations involving thin boundary layers. We now provide a brief overview of the DES model as implemented in the Spalart-Allmaras turbulence model. More detailed discussions can be found in References [8, 10, 11, 22].

In the Spalart-Allmaras model, the wall destruction term is taken to be proportional to $(\tilde{\nu}/d)^2$ where $\tilde{\nu}$ is a working variable related to the turbulent viscosity and d is the distance to the nearest wall. If local equilibrium occurs and the production and destruction terms are in balance, the eddy viscosity becomes proportional to $\hat{S}d^2$ where $\hat{S}$ is the local strain rate. In the Smagorinsky LES model [23], the subgrid-scale turbulent viscosity is proportional to the local strain rate and the local mesh spacing squared, i.e., $\hat{S}\Delta^2$ where $\Delta = max\,(\Delta x, \Delta y, \Delta z)$. Thus, if the distance to the wall d is replaced by the local mesh spacing Δ, the Spalart-Allmaras model will locally behave like a Smagorinsky LES model. To retain the RANS-type behavior in attached boundary layers, d is replaced by a new variable $\tilde{d} = min\,(d, C_{DES}\Delta)$ where C_{DES} is a constant. Note that when $d << C_{DES}\Delta$, the model is in a RANS mode and models the average properties of attached flow turbulence. When $d >> C_{DES}\Delta$, the model is in LES mode and resolves eddies larger than some wavelength depending on the characteristics of the flow solved and the local mesh spacing. For unstructured meshes, the spacing Δ is taken to be the longest distance between the cell center and neighboring cell centers [22]. The implementation of the DES model has two immediate implications regarding the mesh:

1. The mesh in the boundary layer should be highly anisotropic. In particular, the spacing along the surface should be larger than the local boundary layer thickness. This ensures that the model operates in a RANS mode near the boundary.

2. There is no advantage to having an anisotropic mesh in the interior of the domain. The premise of LES is to filter out only eddies that are statistically isotropic [7] so that equal resolution in all directions is reasonable.

Other implications regarding the discretization of the domain are discussed in the Section 3.3.

3. Numerical Considerations

The prediction of the aerodynamic characteristics of an iced wing is a complex problem that involves several steps. Given a geometric definition of a wing with an ice accretion, these steps must be followed:

- Develop a representation of the surface that is suitable for generating a surface mesh.
- Specify the artificial boundaries needed to define the computational domain, e.g., the outer boundary and the side boundaries.
- Generate a mesh and specify boundary conditions on the bounding surfaces of the computational domain.
- Generate a mesh in the interior of the computational domain.
- Generate a flow solution.
- Analyze the results.

The following sections describe how above steps were accomplished in this effort.

3.1 Problem statement

The specific airfoil section considered during this effort was the GLC305 airfoil section with the 22.5-minute glaze ice accretion which is denoted as the two-dimensional 944-ice shape [16]. The ice shape was extruded to form a rectangular planform wing with an aspect ratio of unity to match the configuration used in the test program [17, 18] and is referred to here as the "extruded wing." Since the wing employed for the test program was mounted between walls, the geometry modeled in this study did not include wing tips. Numerical solutions were compared with experimental data for the following conditions: M=0.12, Re/L=3.8x10^6/m which, with a chord length of 0.9144m, yields Re=3.5x10^6, and angles of attack of $0°$, $2°$, $4°$ and $6°$. The extruded 944-ice shape cases considered here correspond to Run 41 in the experimental data [17, 18].

3.2 Geometry modeling

The GLC305/944-ice shape definition was used as input to ICEG2D [24], a two-dimensional tool that automates geometry modeling and mesh generation for ice accretion predictions. ICEG2D redistributes points on the upper and lower surfaces of the defined airfoil using a curvature-based equidistribution algorithm to ensure a sufficient number of points are employed in regions of the airfoil surface with high curvature. A structured surface mesh was then extruded from the section definition. This surface mesh was then converted to a meshing-ready NURBS representation using the mesh generation software GUM-B [25].

3.3 Mesh Generation: Estimated DES zones for iced wing

It is well known that the quality of the CFD solution depends on an appropriate mesh with sufficient mesh density in regions of high flow gradients. In an unsteady flow dominated by convecting vortices, these vortices must be resolved in addition to attached boundary layers. Indeed, as noted by Spalart [7], "*DES compounds the gridding difficulty by incorporating both types of turbulence treatment in the same field.*" Spalart provides guidance as to how a domain should be discretized for DES modeling. He identifies several different regions with different meshing requirements:

- An **Euler region (ER)** is a region that is free of turbulence and vorticity unless it is penetrated by a shockwave. The ER covers most of the domain and an isotropic mesh can be employed in this region.
- A **RANS region (RR)** is primarily composed of the boundary layer where there is no LES content.

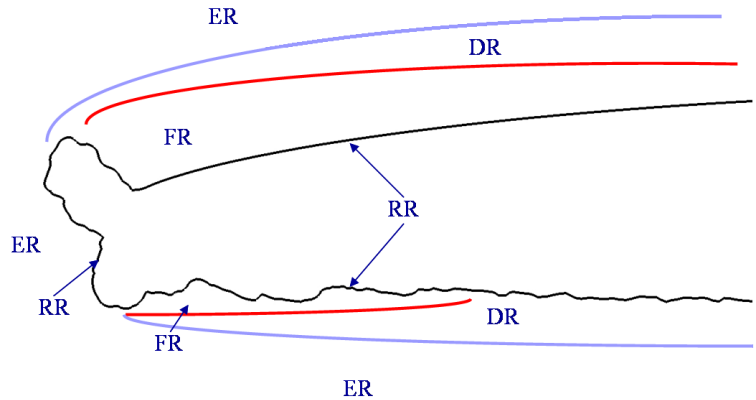

Figure 1: Estimated DES zones for GLC305 airfoil section with two-dimensional 944-ice shape (extruded wing)

  - The **viscous region (VR)** is located within the RANS region and its meshing requirements are similar to those of standard RANS computations.
  - The **RANS outer region (OR)** should be discretized with a mesh in which the mesh spacing in the direction normal to the wall should not exceed once-tenth the thickness of the boundary layer. This is primarily an issue associated with numerical robustness. In practice, this rule is often violated.

- An **LES region (LR)** contains vorticity and turbulence but is not a boundary layer. Significant LES content is present in an LR.
  - The **focus region (FR)** is the region near the body in which the separated turbulence must be well resolved. The mesh should be isotropic in the FR since the LES mode filters out eddies that are statistically isotropic.
  - The **departure region (DR)** is a transitional region between the FR and the ER. The DR does not need to be resolved as well as the FR.

Here, regions are not distinguished by different equations being applied but by different priorities in the mesh spacing. An efficient mesh for any external flow can be designed with these concepts in mind, but not all are strict requirements. Figure 1 depicts the estimated DES zones discussed above as applied to the flow surrounding the 944-ice shape.

3.4 Selection of mesh spacing in focus region

The procedure described below follows that suggested by Spalart [7]. According to Spalart, a well-adjusted subgrid-scale model should allow energy cascade to the smallest eddies that can be tracked on the mesh. Therefore, for most CFD solvers, an eddy with a wavelength of $\lambda = 5\Delta_0$, where Δ_0 is the local mesh spacing, will be active even though it cannot be highly accurate because it lacks the energy cascade to smaller eddies, and is under the influence of eddy viscosity instead. In other words, if we want to adequately resolve an eddy with wavelength λ, the mesh spacing should be $\Delta_0 = \lambda/5$. In the baseline mesh employed for DES computations, an eddy with a wavelength of 5% of the chord was selected, resulting in mesh spacing in the focus region of 1% of the chord. This wavelength was chosen because the height of the horn is approximately 5% of the chord. Therefore, vortices with approximately the same spatial extent as the

horn height can be resolved in the separated region downstream of the horn. As part of the comparison of the DES results with experimental data, the DES mesh was refined by a factor of two in the focus region.

3.5 Selection of time-step size

Selecting the time-step size for DES computations is challenging. Spalart [20] suggests employing a local CFL number (based on the local flow velocity, the local mesh spacing, and the time step size) of unity in the focus regions (FR), that is $\frac{U_0 \Delta t}{\Delta_0}$=1 where U_0 is the maximum flow velocity in the region. Computed RANS results indicate that the maximum flow velocity over the domain is approximately 40–50% greater than the freestream velocity. For the problem considered here with a freestream velocity of approximately 41.1m/s and a wing chord of 0.9144m, the computation for the time step size yields Δt=0.15ms for the baseline DES mesh. For the refined mesh, Δt=0.075ms. However, as Spalart notes [7], steps a factor of 3/2 or even 2 away in either direction from this estimate cannot be considered as "incorrect." Unfortunately, tests with different time steps rarely give any strong indications toward an optimal value [7]. Thus, some ambiguity remains in the selection of the time step size. Solutions were therefore obtained on the baseline DES mesh using the smaller time step to test the effects of reducing the time step size for a fixed mesh.

3.6 Unstructured mesh generation using SolidMesh and VGridns/GridTool

Three different meshes were generated for the extruded wing configuration: a relatively coarse mesh that was used solely for RANS computations, a baseline DES mesh, and a refined DES mesh. The coarse RANS mesh was generated using SolidMesh. SolidMesh is an interface to the unstructured surface and volume mesh generation software AFLR2 and AFLR3 [26]. AFLR3 uses an advancing front algorithm to insert a point in the mesh. The point insertion is followed by a local reconnection to improve mesh quality. The baseline DES and refined DES meshes were generated using GridTool [27] and VGridns [28]. VGridns uses an advancing layer algorithm to generate a tetrahedral volume mesh. The near-body elements of these all-tetrahedral meshes were converted into prisms using the Blacksmith utility [29] thereby producing a mixed element hybrid mesh. SolidMesh produces a hybrid mesh with prisms and tetrahedra automatically. These hybrid meshes were employed because of their potential for improved efficiency and accuracy in comparison to unstructured tetrahedral meshes. The GridTool/VGridns combination was chosen for the DES meshes because it gives the user reasonably good control of the point spacing on the wing surface and the flow field through the use of "sources."

Figure 2 shows the source arrangement for the GLC305 wing with the 944-ice shape. Mesh refinement can be obtained simply by reducing the magnitude of the sources in appropriate regions. In this case, the mesh was locally refined by reducing the source strengths in the upper surface FR by a factor of two while holding the other source strengths constant. This was found to be a reasonably efficient mechanism for mesh refinement for this problem. Since the focus of this effort was the flow on the upper surface, the lower surface mesh was made relatively coarse in comparison. This is indicated by the relative sizes of the midchord source elements for the upper and lower surfaces in Figure 2.

Figures 3(a), 3(b), and 3(c) show cross sections through the coarse RANS, baseline DES, and refined DES meshes respectively. These figures show cutting planes so that the line segments represent intersections of cell faces with the cutting plane. The connectivity of the mesh is evident and the tetrahedra/prism layers near the surface are clearly visible. Figure 3(a) shows the faceted surface represented by the triangular surface mesh on the extruded wing. Additionally, due to the manner in which the spacing is controlled in SolidMesh, there is a spanwise variation in the spacing. The volume mesh in the region downstream of the upper horn is relatively coarse. Refining the surface mesh reduces the faceting and improves the mesh density in the region where flow separation is anticipated, as shown in Figures 3(b) and 3(c). Also note the finer resolution in the focus region downstream of the horn for the refined mesh. These figures also illustrate the connection between the surface mesh and volume mesh. Because of the manner in which the mesh is generated, i.e., anisotropic tetrahedra/prisms transitioning to isotropic tetrahedra, the surface mesh

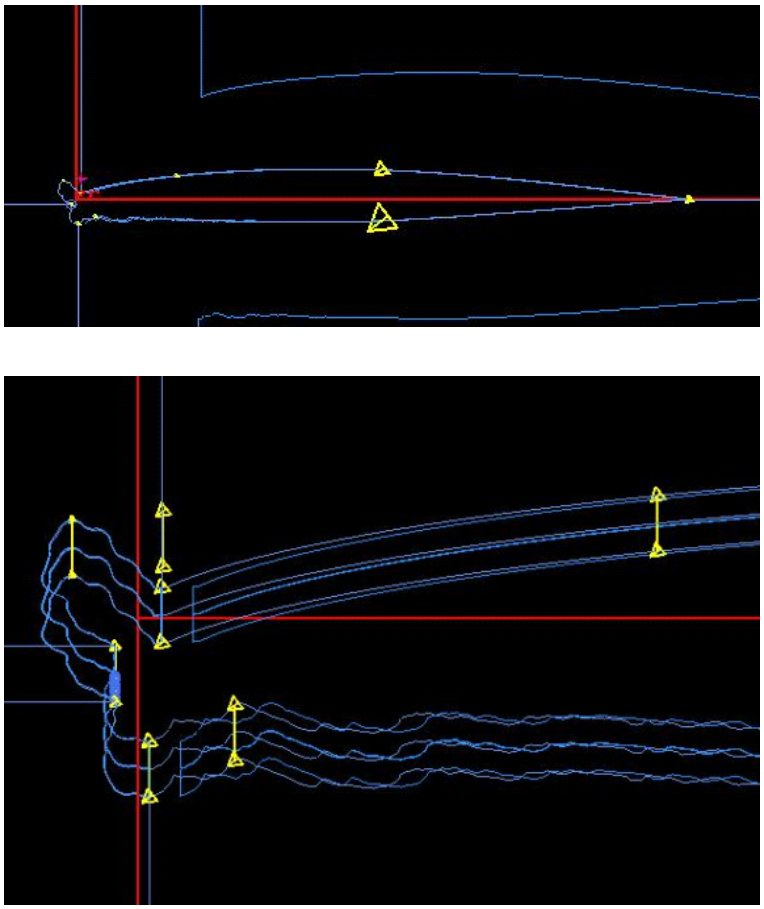

Figure 2: "Sources" used by GridTool/VGridns to generate mesh

characteristics are propagated into the volume mesh. Therefore, in order to refine the mesh spacing in the domain, it is necessary to refine the mesh on the surface.

The meshes shown in Figures 4(a) and 4(b) were used for the two-dimensional computations. Steady state two-dimensional RANS and unsteady two-dimensional DES solutions were obtained on the baseline mesh shown in Figure 4(a) and the refined mesh shown in Figure 4(b). The meshes employed for the two-dimensional simulations were generated by extracting the surface mesh in the symmetry plane from the three-dimensional meshes.

Table 1 shows statistics for the five meshes employed to generate the results reported here. Notice that the localized mesh refinement in the refined DES mesh produces more than a 25% increase in the number of cells when compared to the baseline DES mesh. In some sense, this mesh refinement can be thought of as a manual, albeit crude, attempt at solution adaptive meshing. In all cases, the distance to the first point off the wall was defined so that an average y^+ value less than 0.5 was obtained. This value is well within the recommended values for the turbulence model employed.

3.7 Flow solution

The flow solver employed in this effort is the non-commercial version of Cobalt$_{60}$ [30], which is now called AVUS to reduce confusion with the commercial flow solver. The AVUS flow solver was designed for general unstructured meshes. It employs a nonlinear Riemann solver for the inviscid flux computations and

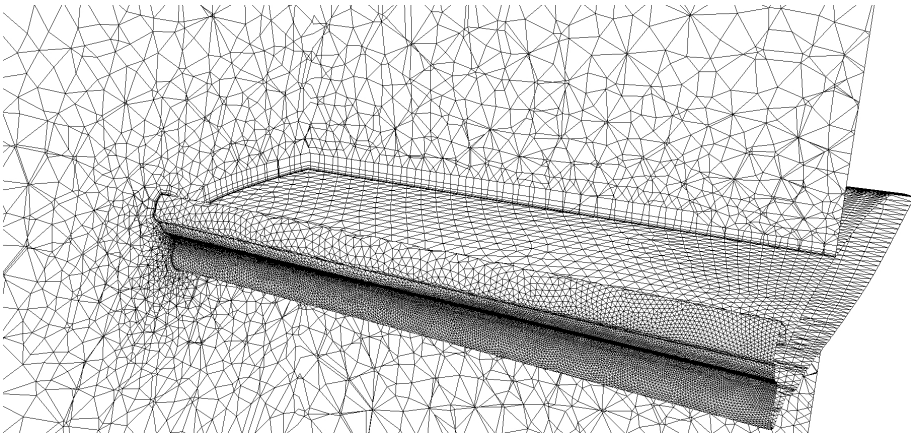

(a) Coarse RANS mesh for extruded wing

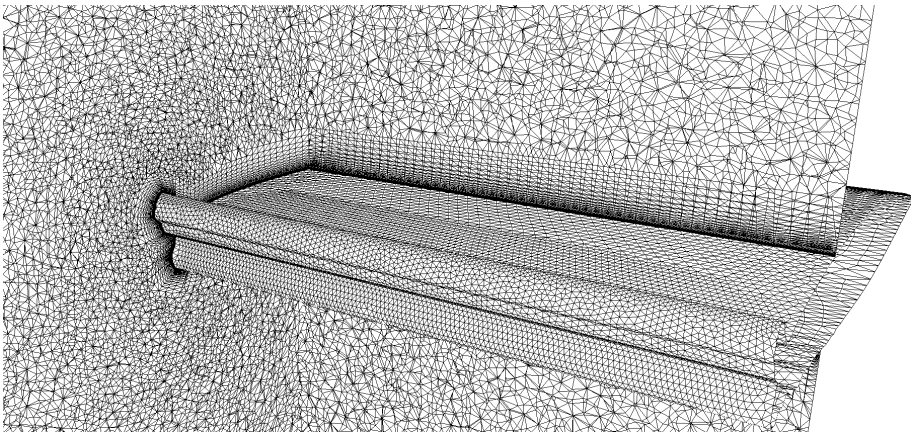

(b) Baseline DES mesh for extruded wing

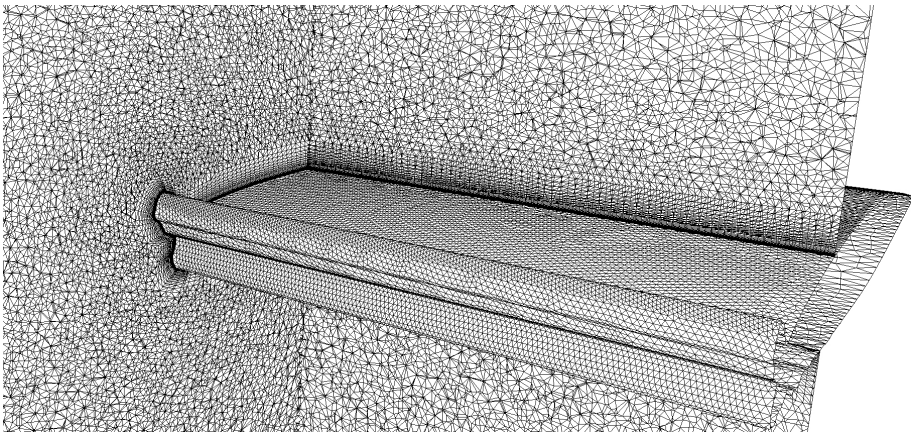

(c) Refined DES mesh for extruded wing

Figure 3: Mesh in cutting planes for extruded GLC305/944-ice shape (extruded wing)

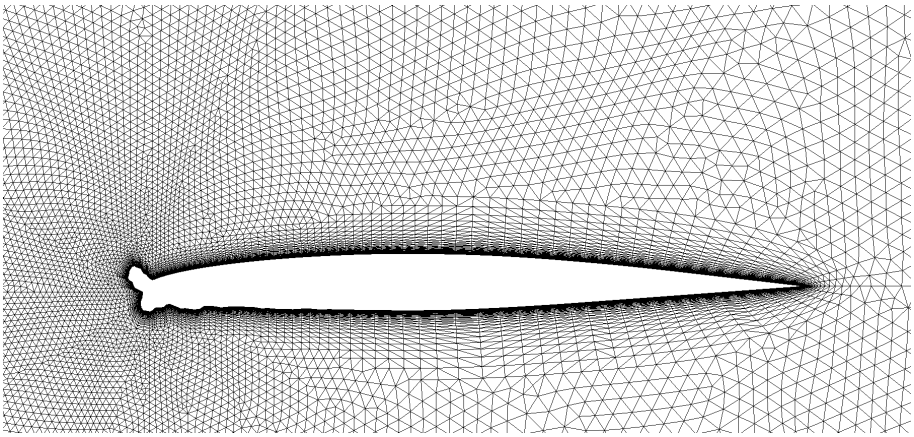

(a) Two-dimensional baseline mesh

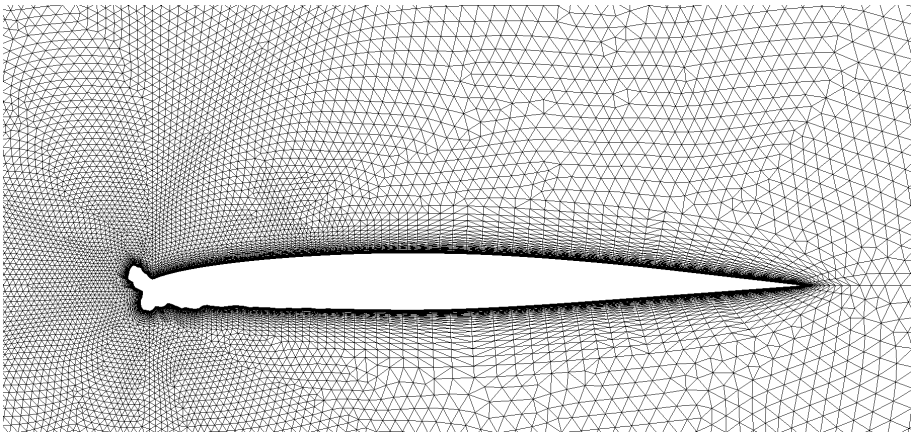

(b) Two-dimensional refined mesh

Figure 4: Two-dimensional mesh for GLC305/944-ice shape

can be run either in explicit or implicit mode. Second-order spatial accuracy is obtained using a linear least-squares reconstruction of the data. The detailed computational methodology used in AVUS is described in reference [19].

All computations were performed using second-order spatial accuracy. The RANS solutions reported here were obtained using first-order, implicit local time stepping and do not in any way represent time-accurate solutions. For the DES computations, the second-order temporal integration scheme was employed. It should be noted that a CFL number of unity in the focus region yields a CFL number on the order of 100,000 in the boundary layer. Therefore, for stability reasons, it was necessary to use the fully-implicit integration scheme ($\theta = 1$) for the DES computations. Based on recommendations in the Cobalt_{60} user's manual [29], two Newton iterations, each consisting of 30 Gauss-Seidel iterations, were employed per time step. Several turbulence models are available including the Spalart-Allmaras one-equation model [20], which was used for the computations reported here. No transition point was specified, and the flow was assumed to be fully turbulent. A slip boundary condition was applied on the artificial side boundaries to reduce computational expense.

Table 1: Statistics for the meshes employed in this effort

	# Nodes	# Faces	# Cells
Extruded Wing (coarse RANS mesh)	890,958	5,299,738	2,258,447
Extruded Wing (baseline DES mesh)	1,828,711	17,327,367	8,341,019
Extruded Wing (refined DES mesh)	2,394,393	22,088,508	10,579,834
Two-dimensional (baseline DES mesh)	26,456	48,775	N/A
Two-dimensional (refined DES mesh)	28,656	52,128	N/A

4. Results

This section presents detailed comparisons with experimental data [17, 18] of the steady RANS and unsteady DES results obtained for the extruded wing (GLC305/944-ice shape). In section 4.1, details of the experiments employed for validation are presented. Comparisons of results obtained from the three-dimensional RANS simulations with experimental data for the extruded wing are given in section 4.2. The results obtained from two-dimensional and three-dimensional DES results are compared with experimental data in section 4.3.

The RANS simulations were performed using an impulsive start and were continued until the normal force reached an approximate steady state, which typically required 15,000–16,000 global iterations. The RANS solutions were then used as initial conditions for the DES computations. The sudden change in the eddy viscosity (due to the reduction in the length scale when the DES computation is initiated) represents a non-physical transient that must be eliminated. Therefore, in all cases, DES computations were performed for 0.75s (a nondimensional time of 33.7), which corresponds to 5000 steps for Δt=0.15ms and 10000 steps for Δt=0.075ms to eliminate this transient. Data was then collected during an additional 0.75s for a total nondimensional time of 67.4 beyond the steady RANS solution.

All cases reported in this effort were run on 64 processors on the EMPIRE cluster or the MAVERICK cluster at the ERC at Mississippi State University. The EMPIRE cluster is a supercomputer class cluster of workstations consisting of 1038 one GHz or better Pentium III processors each with one or more GB of RAM. The MAVERICK cluster is also a supercomputer class cluster comprised of 192 IBM x335 nodes. Each node contains dual 3.06 GHz Xeon processors and 2.5 GB of RAM. We now provide timing data for the runs performed using the EMPIRE cluster. Simulations performed on the MAVERICK cluster required approximately one-half of the time of those performed on the EMPIRE cluster.

For the three-dimensional RANS solutions on the "baseline DES mesh," 1 hour and 39 minutes were required for each 100 iterations on the EMPIRE cluster, whereas 2 hours and 23 minutes were required for each 100 iterations on the "refined DES mesh." Therefore, a steady RANS computation for a single angle of attack required approximately 250 hours on the "baseline DES mesh" and 350 hours on the "refined DES mesh." Here, hours refers to CPU hours.

For the three-dimensional DES computations, 2 hours and 52 minutes were required for 100 time steps on the "baseline DES mesh." Three hours and 52 minutes were required for each 100 time steps on the "refined DES mesh." DES computations using the standard time step for the refined mesh, i.e., Δt=0.075ms, were performed for 20000 time steps and required a total of approximately 575 hours for the "baseline DES mesh" and 775 hours for the "refined DES mesh." Thus, including the time required to compute the converged RANS simulations from which the DES computations were initiated, approximately 820 hours were required to compute the DES results for one angle of attack on the "baseline DES mesh." Approximately 1125 hours were required to compute the DES results for a single angle of attack on the "refined DES mesh."

4.1 Experimental details

Addy *et al.* [17] performed icing effects studies for a 36-inch chord, two-dimensional business jet airfoil (GLC305) by conducting wind tunnel tests in NASA Langley Research Center's LTPT. The GLC305 airfoil is designed for low transonic drag and has a maximum thickness to chord ratio of 8.7%. Four different types of ice shapes were considered for this study. Ice shapes were accreted on the GLC305 airfoil in the IRT over a range of icing conditions selected from the FAA FAR Part 25-Appendix C [31]. The 22.5-minute glaze 944-ice shape was one of the ice shapes considered. The Reynolds numbers ranged from $3.0\text{x}10^6$ to $10.5\text{x}10^6$ at a fixed Mach number of 0.12. The effects of Mach number variation (0.12 and 0.28) were investigated at constant Reynolds numbers of $6.0\text{x}10^6$ and $10.5\text{x}10^6$.

The airfoil model was supported horizontally across the width of the test section between two 40-inch diameter circular end-plates. These end-plates were flush mounted with the sidewalls and rotated to provide

the angle of attack adjustment. Each end-plate was equipped with a porous section for sidewall boundary layer control. The lift and pitching moment data were obtained from the integration of surface static pressures, while the drag coefficients were calculated using the standard momentum deficit method based on the pressures measured using a wake probe. Corrections to the integrated performance coefficients accounting for solid and wake blockage and streamline curvature were applied to the data during post processing.

Figures 5(a) and 5(b) depict comparisons of the lift and drag coefficients, respectively, for the clean and the extruded wings. Figure 6 shows the pressure coefficient for the clean and extruded wings for an angle of attack range of 0° to 6° in 2° increments. The data shown here was obtained at a Mach number of 0.12 and a Reynolds number of $3.5\text{x}10^6$ for the extruded wing case while the clean wing data was obtained at the same Mach number and a Reynolds number of $3.0\text{x}10^6$.

Broeren *et al.* [18] also carried out flow field measurements on the upper surface of the same model. Data were obtained at three different angles of attack preceding stall at Reynolds numbers of $3.5\text{x}10^6$ and $6.0\text{x}10^6$ and Mach numbers of 0.12 and 0.21. Split-hot-film anemometry was used to measure the time-averaged flow velocities and its RMS fluctuations. Results confirmed the presence of a large separation bubble downstream of the ice shapes. Figure 7 shows experimental time-averaged streamwise velocity plots for the extruded wing at angles of attack of 0°, 4° and 6°. In general, these time-averaged velocity contour images provide a good overall illustration of the separated flow past the ice shape. From these images, we can see how the boundary layer separates near the tip of the ice horn. A significant reversed flow region is also formed below the separated shear layer.

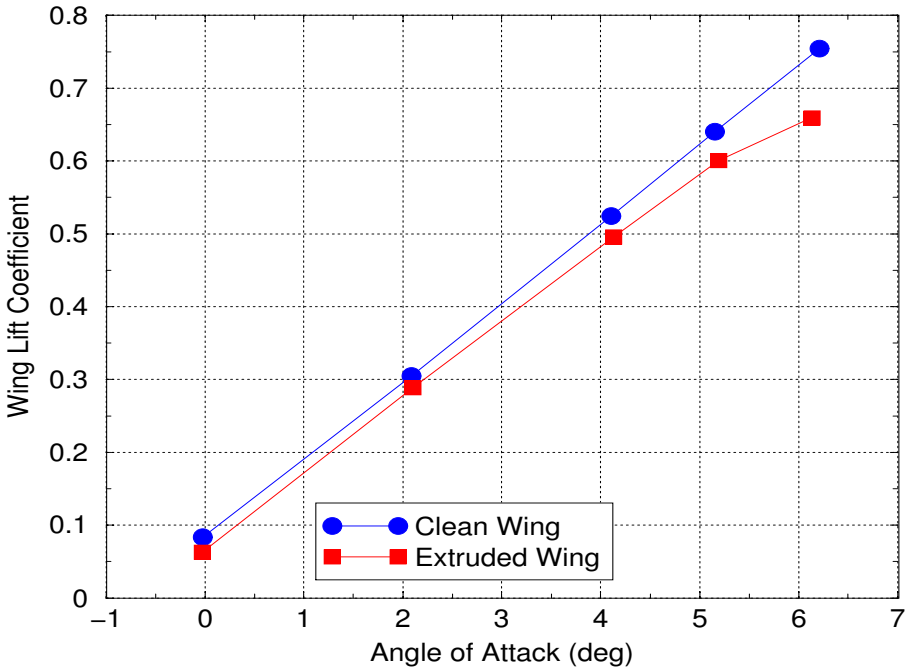

(a) Experimental lift coefficients

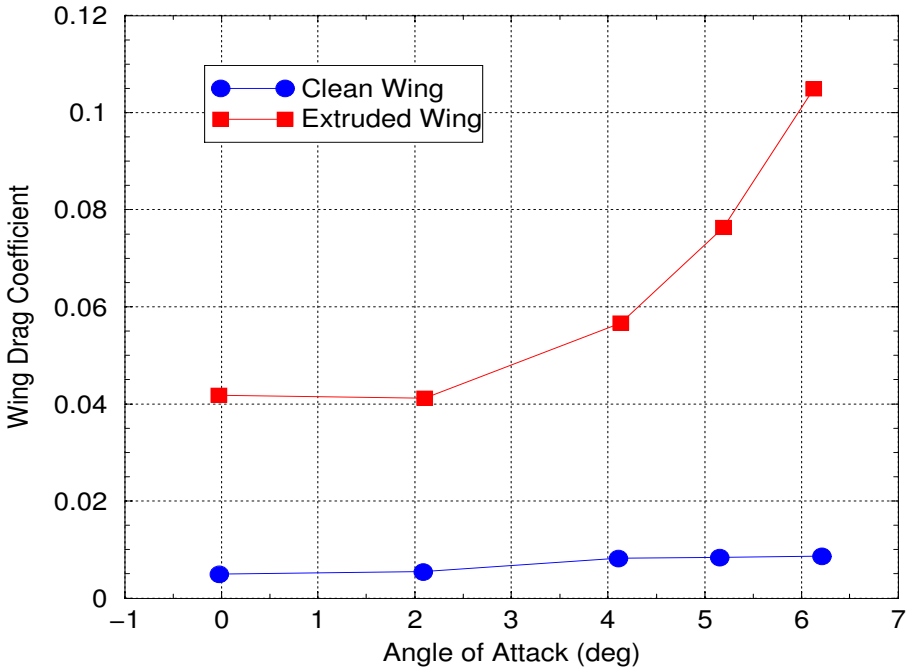

(b) Experimental drag coefficients

Figure 5: Comparison of experimental lift and drag coefficients for extruded GLC305 airfoil section: with and without 944-ice accretion [17]

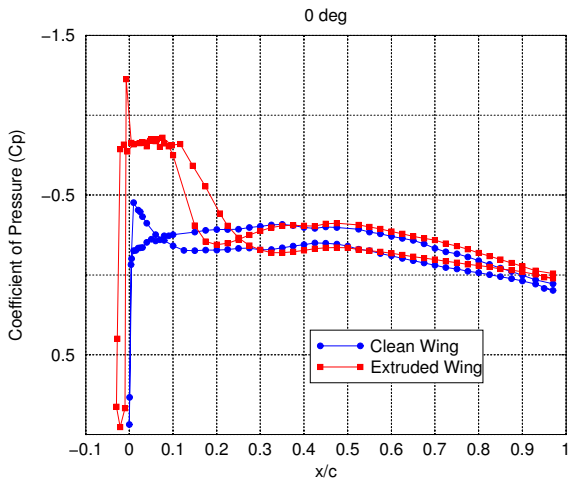

(a) 0° angle of attack

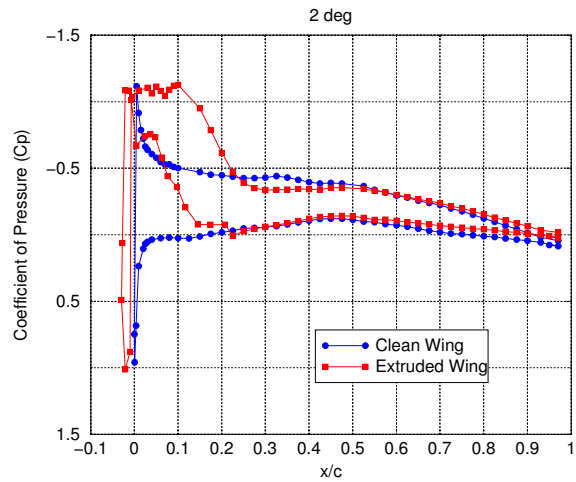

(b) 2° angle of attack

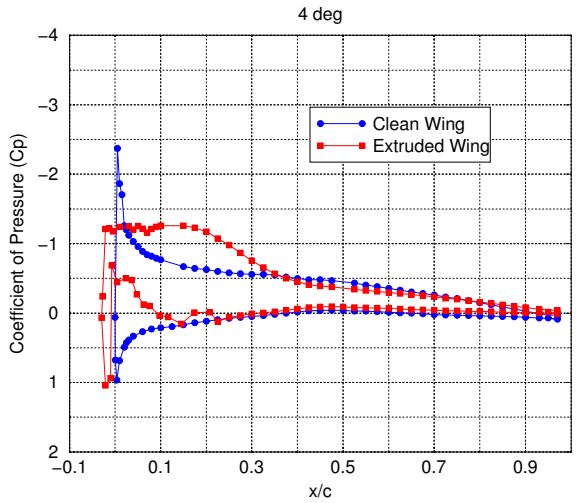

(c) 4° angle of attack

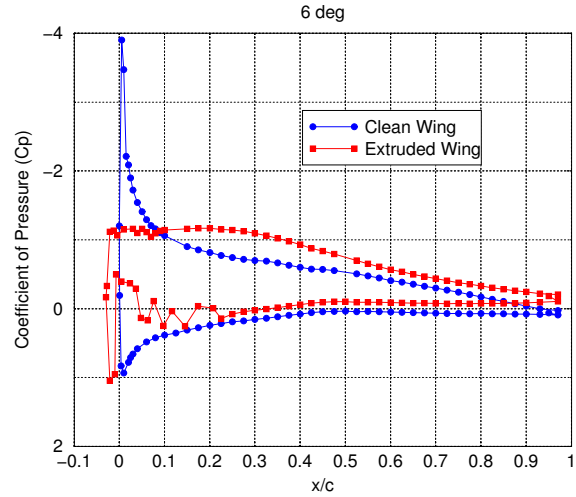

(d) 6° angle of attack

Figure 6: Comparison of experimental pressure coefficients for extruded GLC305 airfoil section: with and without 944-ice accretion [17]

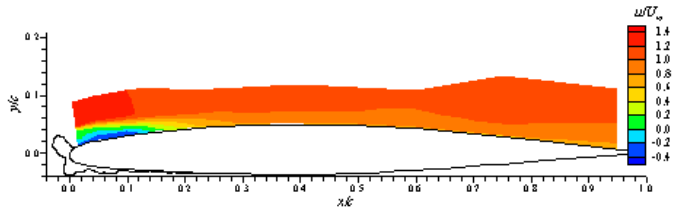

α=0°

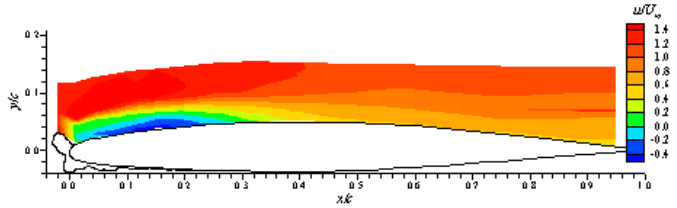

α=4°

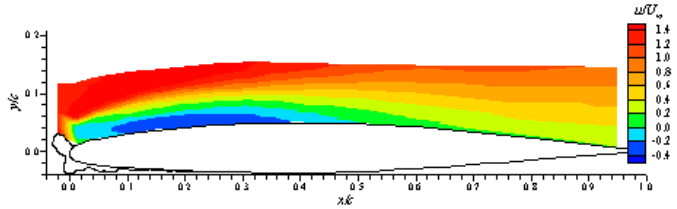

α=6°

Figure 7: Experimental u-velocity contours for the extruded wing at angles of attack of $0°$, $4°$ and $6°$ [18]

4.2 RANS results

In this section, steady RANS results obtained for the extruded wing are compared with experimental data [17, 18]. RANS computations were performed on the meshes denoted as "coarse RANS," "baseline DES," and "refined DES," shown in Figures 3(a), 3(b) and 3(c), respectively, at angles of attack of $0°$ to $6°$ in $2°$ increments. For angles of attack of $0°$ and $2°$, 14,000 iterations were performed on the baseline DES mesh and refined DES mesh. For angles of attack of $4°$ and $6°$, 16,000 iterations were performed on both the baseline and refined DES meshes. Results are also included for the two-dimensional simulations for reference.

Figure 8 shows the convergence histories for the extruded wing computation for an angle of attack of $6°$ using the baseline DES mesh. The lift force and axial force reached asymptotic values indicating a converged solution as shown in Figures 8(a) and 8(b), respectively. The $6°$ convergence history is representative of the computations for other angles of attack using this mesh.

Figure 9 shows comparisons of the wing lift and drag coefficients computed from the steady RANS simulations with experimental data for an angle of attack range of $0°$ to $6°$ in $2°$ increments. As shown in Figure 9(a), the lift coefficient at $0°$ shows good agreement with experimental data for all cases, although the two-dimensional cases are somewhat underpredicted. However, as the angle of attack increased, the deviation between the predicted lift and experimental values increased. The lift is underpredicted relative to the experimental data. Additionally, the premature break in the predicted lift curve slope, characteristic of the "near stall" behavior of the wing, suggests that the predictions are overestimating the severity of the flow separation. As shown in Figure 9(b), the predicted drag coefficient shows reasonable agreement with the experimental data. This relatively good agreement (for drag) can be attributed to the fact that the drag is primarily composed of form or pressure drag for this configuration, i.e., the ice shape is a bluff body. However, the good agreement between the results predicted using the coarse RANS mesh and the experimental data appears to be somewhat fortuitous. The agreement is not as good for predictions made using the baseline DES mesh and refined DES mesh.

Figures 10-13 show comparisons of the predicted midspan pressure coefficients for the three-dimensional steady RANS simulations with experimental data for an angle of attack range of $0°$ to $6°$ in $2°$ increments. It should be noted that, for each case considered, there were only minimal spanwise variations in the pressure distribution. At the lower angles of attack, neither the upper or lower surface pressure distributions agree well with experimental data in the first 30% of the chord. As the angle of attack increases, the agreement between the lower surface predictions and experimental data improves. The discrepancies between the upper surface predictions and the experimental data increase. This can be explained as follows. At the lower angles of attack, the upper and lower surface horns present nearly "equal" disturbances to the flow field. As the angle of attack increases, the lower surface horn presents less of a disturbance while the upper surface horn presents more of a disturbance. Thus, an increasing angle of attack produces a decreasing region of separated flow on the lower surface and an increasing region of separated flow on the upper surface. One characteristic that is present in each case is the pressure overshoot that occurs just downstream of the upper and lower surface horns. The pressure near the stagnation region appears reasonably well-predicted. On both the upper and lower surfaces, the flow accelerates around the horn tip, as indicated by the pressure drop. A sudden recompression occurs to a pressure level that is too high. The cause of this behavior is not currently known. It should be noted that the two-dimensional steady RANS results report by Chi, et al. [21] show a different behavior. In the results shown in Ref. [21], better agreement is obtained near the horn. The agreement then deteriorates as you move downstream. These results suggest that it is possible that the discrepancies shown in Figures 10 through 13 may be due to an overall lack of resolution of the horn tip. However, mesh refinement studies by Chung, et al. [32] suggest that the streamwise mesh spacing has only minimal impact on solution accuracy for iced wing flow fields. This point is currently being investigated. We can also note that, in general, mesh refinement produces some improvement from the coarse mesh to

the baseline mesh, when compared to the experimental data. No significant improvement is noted, however, after refinement from the baseline mesh to the refined mesh.

Figures 14-16 show comparisons of the predicted x-component of velocity for the three-dimensional steady RANS simulations with experimental data for angles of attack of $0°$, $4°$, and $6°$. Using these images, the reattachment location of the primary upper surface flow separation may be estimated by locating the position on the chord at which the u=0 contour intersects the upper surface of the wing. At an angle of attack of $0°$, the reattachment position is well predicted on the coarse, baseline, and refined meshes. As the angle of attack is increased to $4°$, the downstream extent of the separated region is slightly overpredicted, approximately 32% of the chord as compared to 28% of the chord. As the angle of attack is further increased to $6°$, the extent of the separated region is significantly overpredicted and the upper surface reattachment position is shifted downstream until the flow is completely separated. The experimental data shows a flow reattachment at approximately 52% of the chord. Although mesh refinement does improve the prediction relative to the coarse mesh for both the $4°$ and $6°$ angle of attack solutions, no significant improvements are observed when comparing results computed on the baseline and refined meshes. Additionally, at both $4°$ and $6°$, the transverse extent of the reversed flow region appears to be underpredicted (bubble appears to be thicker in the experimental velocity contours). The extra dissipation present in the coarse mesh is evident from the increased spreading of the shear layer in comparison to results predicted using the baseline and refined mesh. However, this spreading is not as severe as expected given the relative coarseness of the coarse mesh. The seemingly anomalous velocity contours that appear in the experimental data just downstream of the horn are artifacts from the process employed to generate the contour plots.

Figures 17–20 show predictions of separation (red) and attachment (blue) locations for an angle of attack range of $0°$ to $6°$ in $2°$ increments for the coarse RANS mesh, baseline DES mesh, and refined DES mesh, respectively. The technique of Kenwright [33] is employed to locate surface mesh elements in which a potential separation or attachment line crosses. No attempt is made to reconstruct the actual curves. Kenwright's technique is based on a phase plane analysis of critical points in the velocity field "close" to the surface and, as such, is subject to anomalous results if there is noise in the data. The baseline and refined mesh results show fairly well resolved flow features including secondary chordwise separations and corresponding attachments clearly indicated just down stream of the horn (the closely spaced, roughly parallel blue and red curves located just aft of the leading edge). The refined mesh results show a relatively uniform primary reattachment across the span in each case. The coarse mesh does not resolve this secondary separation at any angle of attack. Additionally, the location of the primary reattachment predicted using the coarse mesh does not exhibit the same uniformity that is present in the baseline and refined mesh computations except for the $6°$ case which is fully separated. It is assumed that the coarser, nonuniform surface mesh employed in the coarse mesh, as shown in Figure 3(a), is responsible for the appearance of the coarse mesh flow fields. Conclusions drawn regarding the attachment locations are consistent with those drawn from the velocity contours for the $0°$, $4°$, and $6°$ cases.

To summarize, the steady-state RANS results show an increasing region of separation on the upper surface as angle of attack is increased. In all cases, pressure overshoots occur downstream of the upper and lower surface horns resulting in an elevated pressure downstream of the horns. In the $4°$ angle of attack results, the downstream extent of the upper surface separation appears slightly overpredicted. In the $6°$ angle of attack results, the flow is fully separated. The velocity contour data further suggest that the transverse thickness of the separated region is underpredicted. The general trend is that mesh refinement does not improve the accuracy of the solution beyond the initial refinement from the coarse mesh to the baseline mesh. No significant improvement is observed after further refinement.

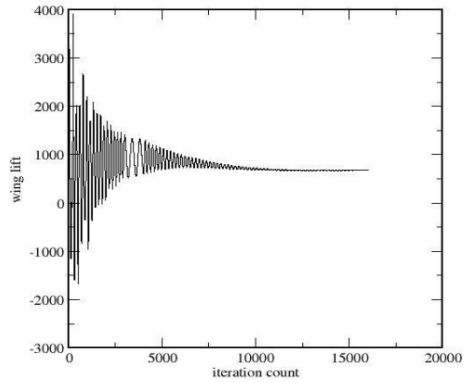

(a) Extruded wing (baseline DES mesh) – lift history

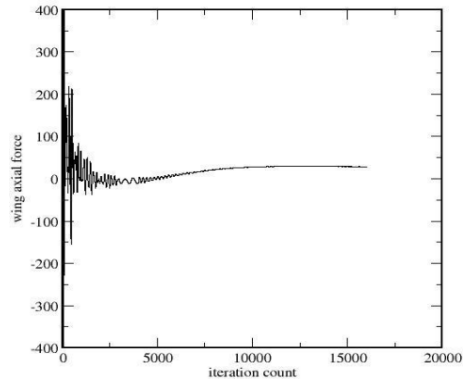

(b) Extruded wing (baseline DES mesh) – axial force history

Figure 8: Convergence of RANS solution for extruded wing (baseline DES mesh at a 6° angle of attack)

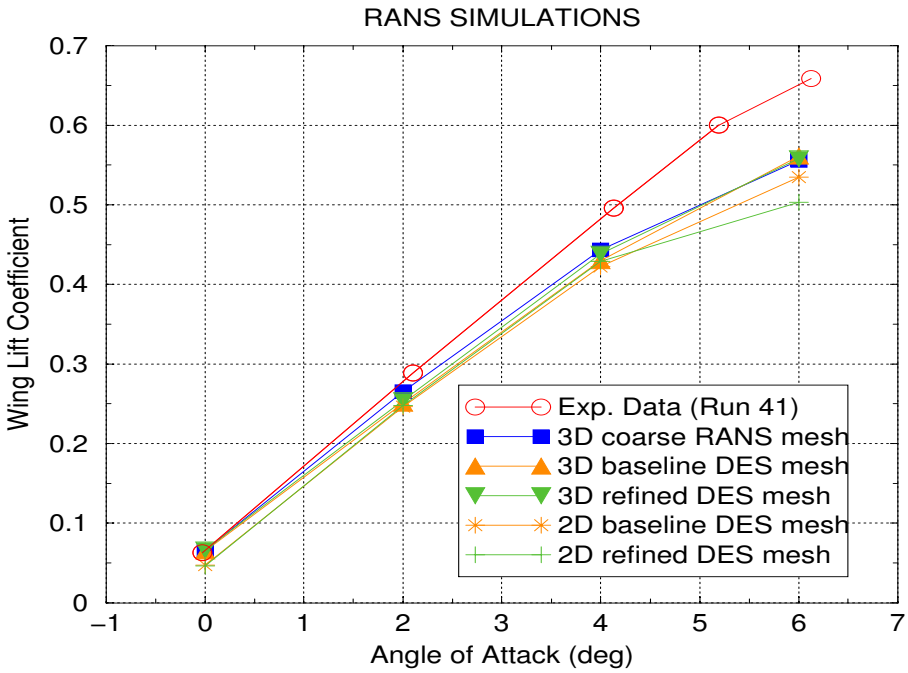

(a) Lift coefficients

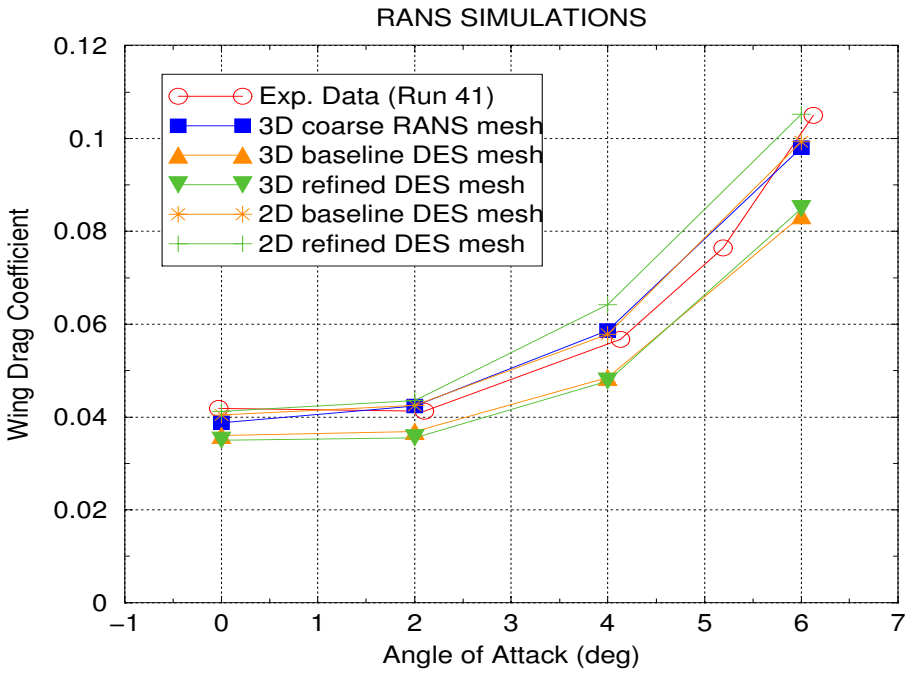

(b) Drag coefficients

Figure 9: Comparison of predicted (RANS) force coefficients and experimental data for the extruded wing (coarse RANS mesh, baseline DES mesh, and refined DES mesh)

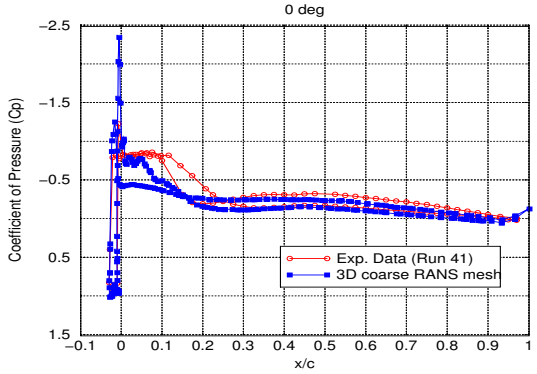

(a) Coarse RANS mesh

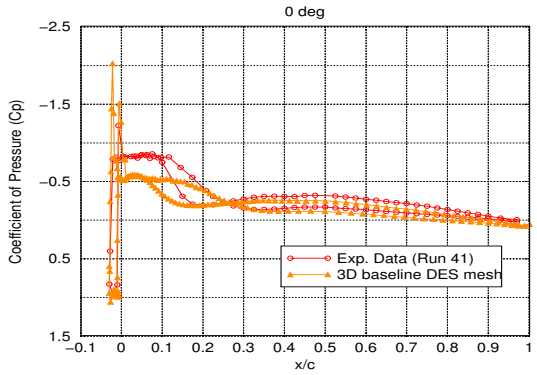

(b) Baseline DES mesh

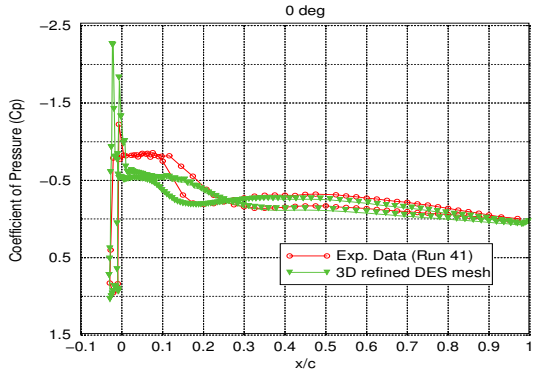

(c) Refined DES mesh

Figure 10: Comparison of predicted (RANS) midspan pressure coefficients and experimental data for the extruded wing at $0°$ angle of attack

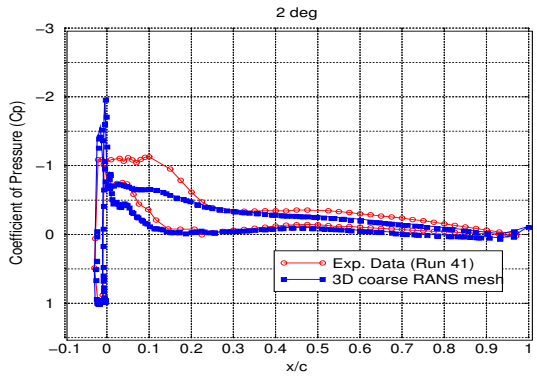

(a) Coarse RANS mesh

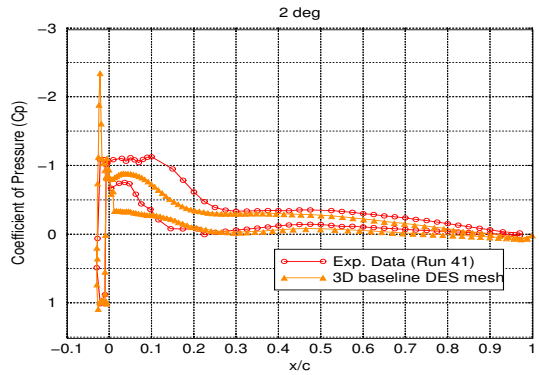

(b) Baseline DES mesh

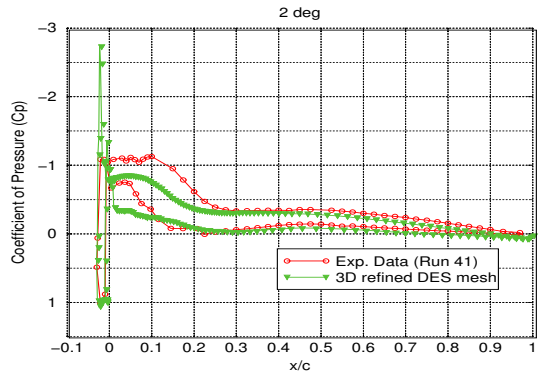

(c) Refined DES mesh

Figure 11: Comparison of predicted (RANS) midspan pressure coefficients and experimental data for the extruded wing at 2° angle of attack

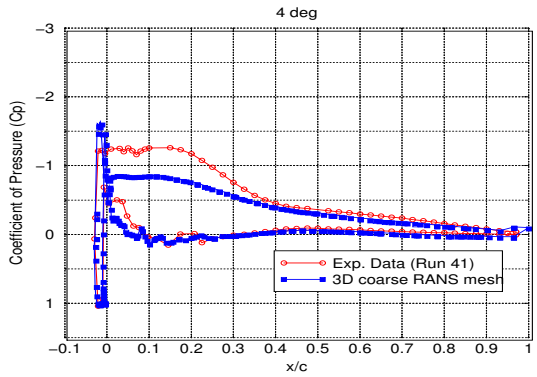

(a) Coarse RANS mesh

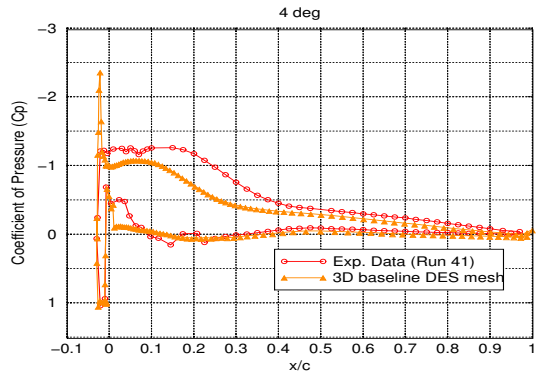

(b) Baseline DES mesh

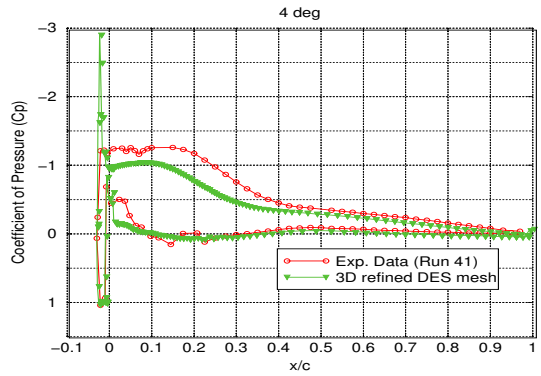

(c) Refined DES mesh

Figure 12: Comparison of predicted (RANS) midspan pressure coefficients and experimental data for the extruded wing at 4° angle of attack

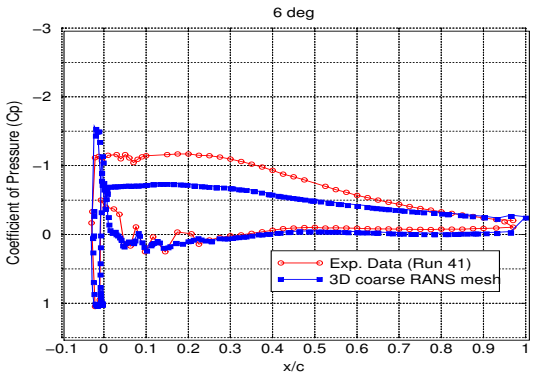

(a) Coarse RANS mesh

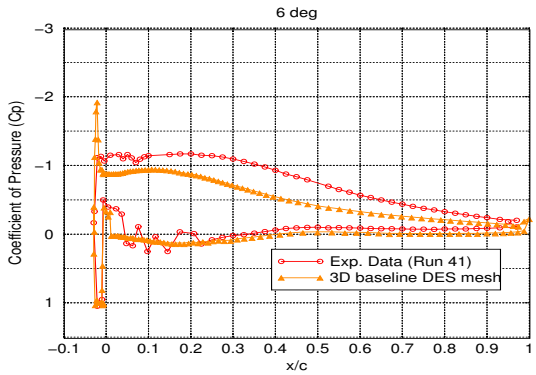

(b) Baseline DES mesh

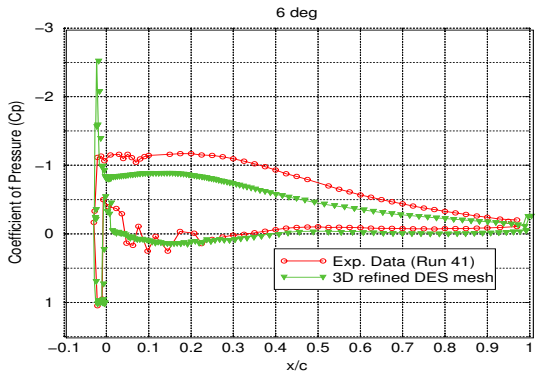

(c) Refined DES mesh

Figure 13: Comparison of predicted (RANS) midspan pressure coefficients and experimental data for the extruded wing at 6° angle of attack

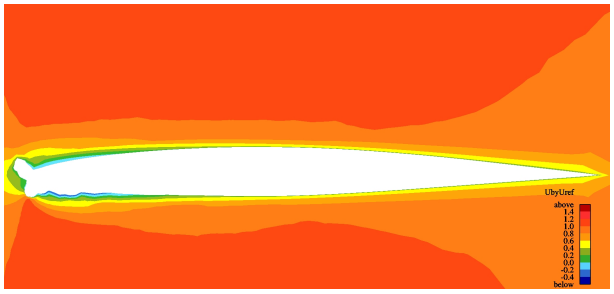

(a) Extruded wing (coarse RANS mesh)

(b) Extruded wing (baseline DES mesh)

(c) Extruded wing (refined DES mesh)

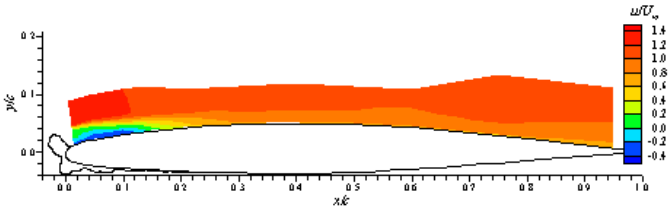

(d) Experimental hot-split-film data

Figure 14: Comparison of predicted (RANS) midspan u-velocity contours and experimental data for the extruded wing at 0° angle of attack

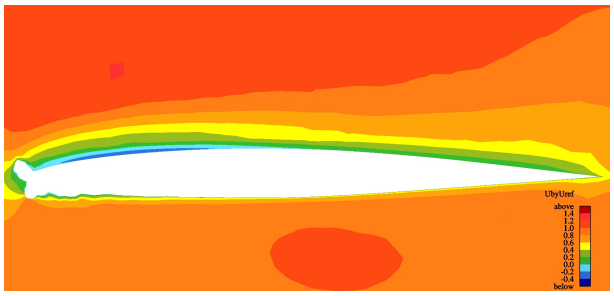

(a) Extruded wing (coarse RANS mesh)

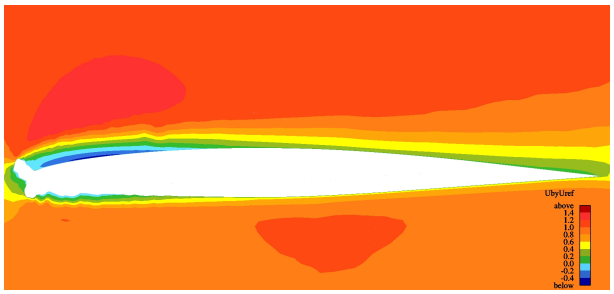

(b) Extruded wing (baseline DES mesh)

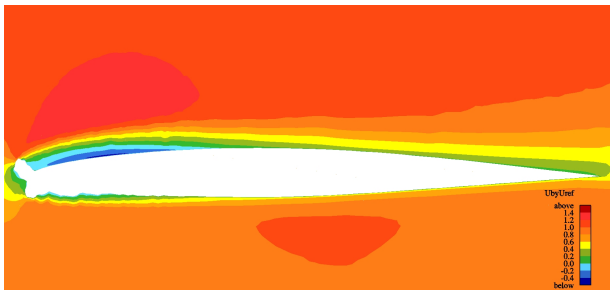

(c) Extruded wing (refined DES mesh)

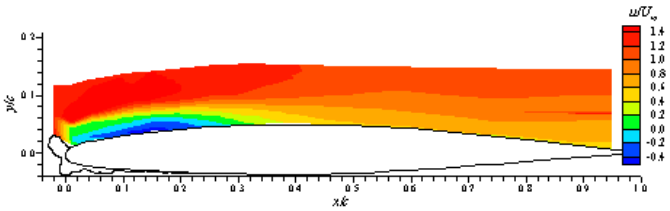

(d) Experimental hot-split-film data [18]

Figure 15: Comparison of predicted (RANS) midspan u-velocity contours and experimental data for the extruded wing at $4°$ angle of attack

(a) Extruded wing (coarse RANS mesh)

(b) Extruded wing (baseline DES mesh)

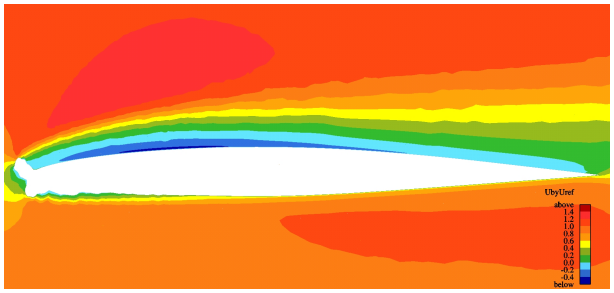

(c) Extruded wing (refined DES mesh)

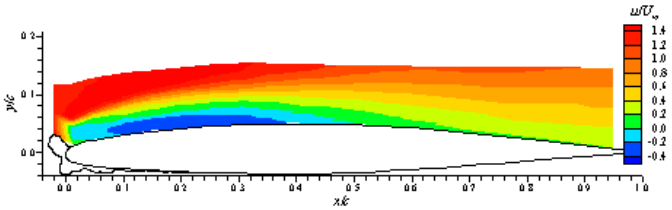

(d) Experimental Hot-Split-Film Data [18]

Figure 16: Comparison of predicted (RANS) midspan u-velocity contours and experimental data for the extruded wing at 6° angle of attack

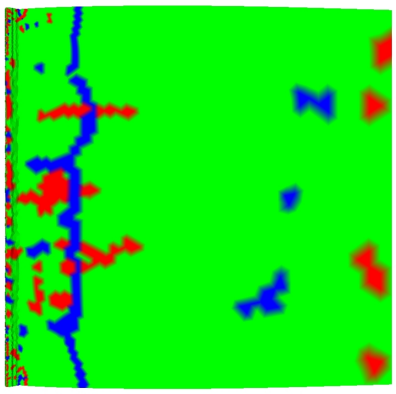

(a) Coarse RANS mesh

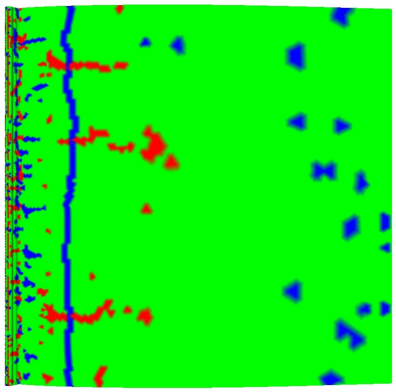

(b) Baseline DES mesh

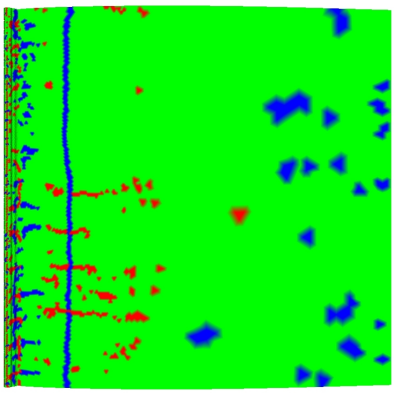

(c) Refined DES mesh

Figure 17: Comparison of predicted (RANS) upper surface separation (red) and attachment (blue) locations for the extruded wing at 0° angle of attack

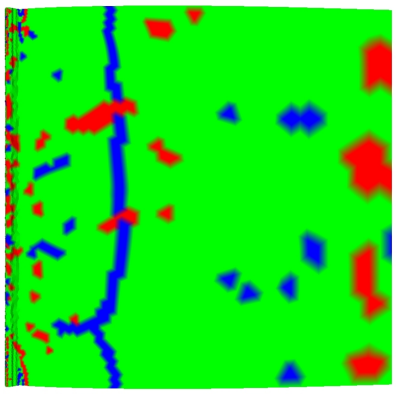

(a) Coarse RANS mesh

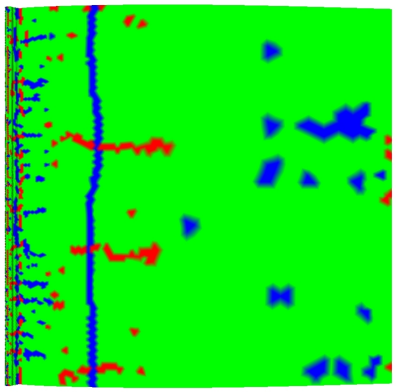

(b) Baseline DES mesh

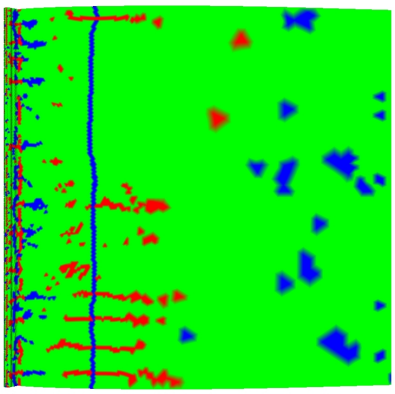

(c) Refined DES mesh

Figure 18: Comparison of predicted (RANS) upper surface separation (red) and attachment (blue) locations for the extruded wing at 2° angle of attack

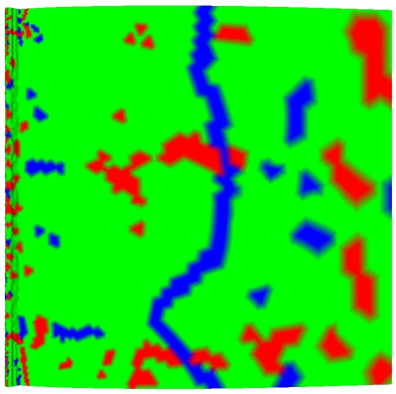

(a) Coarse RANS mesh

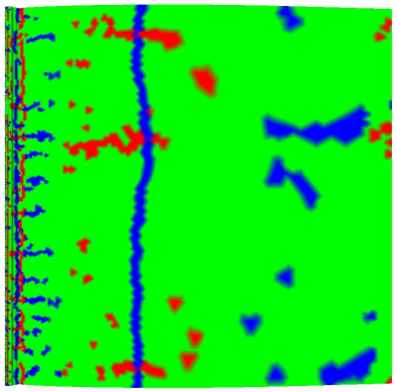

(b) Baseline DES mesh

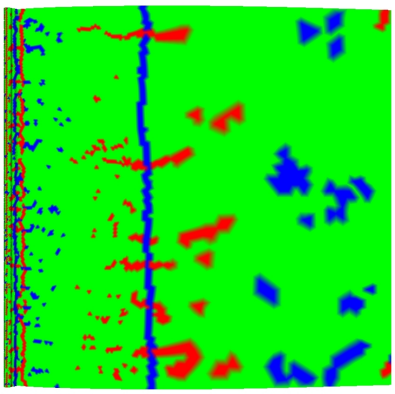

(c) Refined DES mesh

Figure 19: Comparison of predicted (RANS) upper surface separation (red) and attachment (blue) locations for the extruded wing at 4° angle of attack

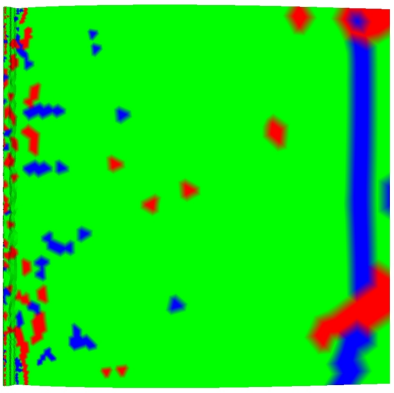

(a) Coarse RANS mesh

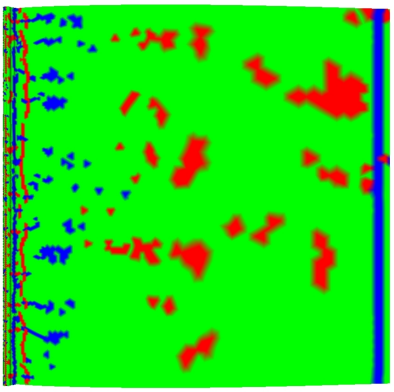

(b) Baseline DES mesh

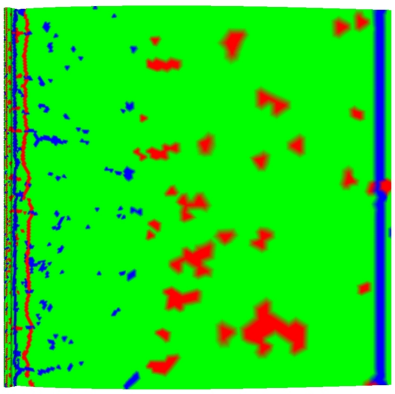

(c) Refined DES mesh

Figure 20: Comparison of predicted (RANS) upper surface separation (red) and attachment (blue) locations for the extruded wing at 6° angle of attack

4.3 DES results

In this section, results from the two-dimensional and three-dimensional DES computations and comparisons with experimental data [17, 18] are presented. Results obtained from mesh refinement and time step studies are also included. In addition to integrated quantities such as lift and drag, we present detailed comparisons for time-averaged and fluctuating quantities. All DES solutions were initiated from converged steady RANS solutions.

4.3.1 Two-dimensional DES results

DES computations were performed on the two-dimensional baseline mesh using several different time steps. The timesteps chosen were Δt=0.6ms, Δt=0.3ms, Δt=0.15ms, Δt=0.075ms, and Δt=0.0375ms at 6° angle of attack. DES computations were also performed on the refined mesh at 4° and 6° angles of attack with Δt=0.075ms. Here, Δt=0.15ms is the time step estimated using the approach described in reference [7] and outlined in section 3.5.

Table 2 shows the time-averaged lift and drag coefficients computed using the baseline DES mesh and several different time steps. Note that the lift and drag coefficients appear to converge for a time step of roughly one-half of the estimated Δt. Figures 21 and 22 show comparisons between two-dimensional DES results and experimental data for the time-averaged x-component of the velocity for angles of attack of 4° and 6° for the baseline and the refined mesh. Figures 21 and 22 show that the two-dimensional DES results overpredict the size of the separated region downstream of the horn. Figures 21 and 22 and Table 2 indicate that the two-dimensional DES results overpredict the force coefficients. Additionally, mesh refinement does not have much effect on the the solution.

Figure 23 shows the instantaneous vorticity plots for t^*=0.3, t^*=33.7 and t^*=67.4. The unsteadiness in the flow and the vortex shedding downstream of the airfoil can readily be observed. Figure 23 shows the ability of DES method to capture the large-scale vortices for this kind of unsteady flow problems.

We attribute the significant differences between the simulation results and the experimental data to the fact that the simulation is two dimensional. As will be seen in the next section, even though there is no spanwise variation in the wing section, the resulting flow field is highly three dimensional. Therefore, we would not expect the two-dimensional simulation to accurately model the conditions in the actual flow field. Similarly anomalous behaviors were observed in two-dimensional DES results by Kumar and Loth [12].

Table 2: Two-dimensional DES time-averaged lift and drag coefficients on the baseline mesh, for different time steps at 6° angle of attack

Time Step	Lift Coefficient (C_L)	Drag Coefficient (C_D)
Experimental (α = 6.124)	0.659	0.105
Δt=0.6ms	0.772	0.144
Δt=0.3ms	0.869	0.172
Δt=0.15ms	0.788	0.154
Δt=0.075ms	0.877	0.165
Δt=0.0375ms	0.878	0.165

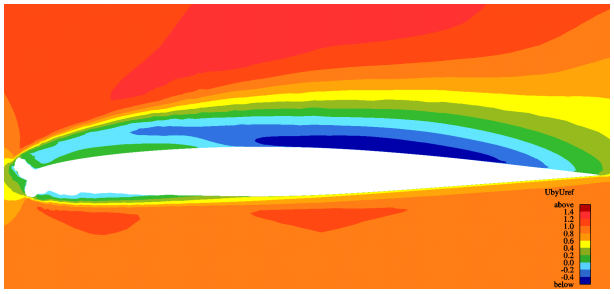

(a) Two-dimensional baseline mesh

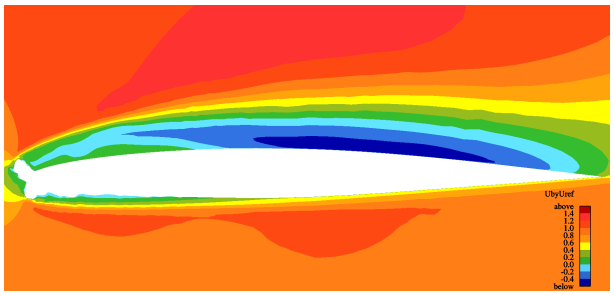

(b) Two-dimensional refined mesh

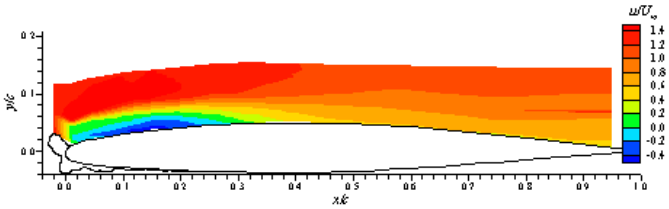

(c) Experimental hot-split-film data [18]

Figure 21: Comparison of predicted time-averaged u-velocity contours and experimental data for the extruded wing (two-dimensional baseline DES mesh, and two-dimensional refined DES mesh at 4° angle of attack with Δt=0.075ms)

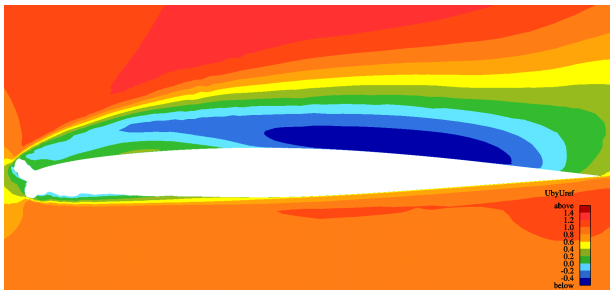

(a) Two-dimensional baseline mesh

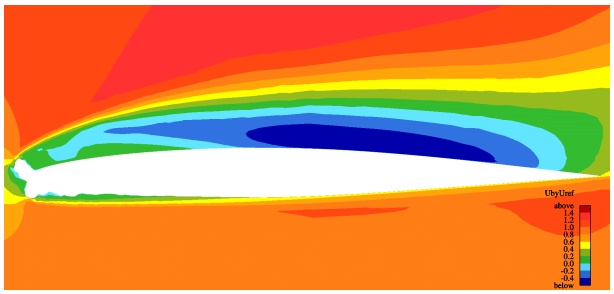

(b) Two-dimensional refined mesh

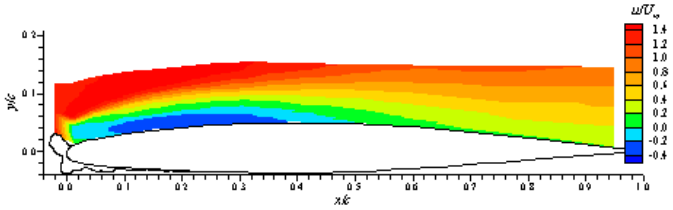

(c) Experimental hot-split-film data [18]

Figure 22: Comparison of predicted time-averaged u-velocity contours and experimental data for the extruded wing (two-dimensional baseline DES mesh, and two-dimensional refined DES mesh at 6° angle of attack with Δt=0.075ms)

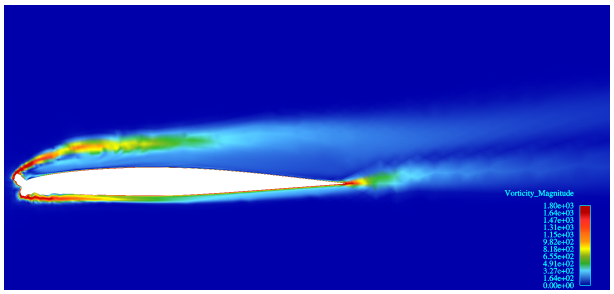

(a) t^*=0.3

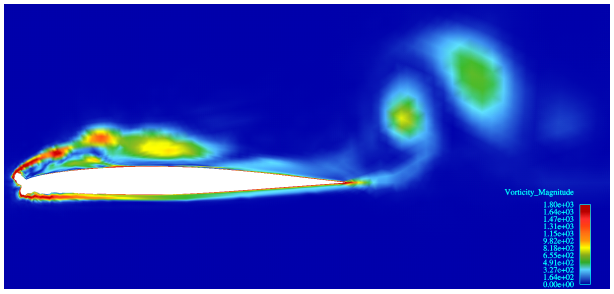

(b) t^*=33.7

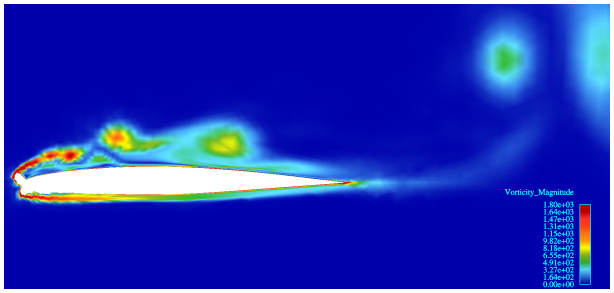

(c) t^*=67.4

Figure 23: Instantaneous vorticity plots for two-dimensional baseline mesh at 6° angle of attack with Δt=0.15ms

4.3.2 *Three-dimensional DES results:* 4° *angle of attack,* Δt*=0.15ms, baseline mesh*

We now compare DES results obtained using the baseline DES mesh with Δt=0.15ms with the experimental data at 4° angle of attack. Table 3 shows a comparison of time-averaged lift and drag coefficients with the corresponding RANS results and experimental data. Differences between the steady RANS results and the time-averaged DES results are less significant.

Figure 24 shows comparisons of the predicted time-averaged DES and steady RANS midspan pressure distribution with experimental data. The time-averaged DES results show a nearly constant pressure from the leading edge to approximately 20% of the chord. This constant pressure region on the upper surface indicates that the flow separates from the horn and forms a separation bubble aft of the ice shape. The steady RANS predictions show a pronounced pressure decrease in the region ahead of the 10% chord location. However, there is no clear constant pressure region. As the flow proceeds aft, the differences between the RANS results and the DES results decrease. There are small differences between the DES results and RANS results on the lower surface ahead of 30% chord. Aft of this point, the predicted pressures are similar and compare favorably to the experimental pressures.

Figure 25 shows a comparison between the RANS results, the DES results, and the experimental data for the time-averaged x-component of the velocity at midspan. The reattachment location on the wing upper surface may be estimated by locating the position on the chord at which the u=0 contour intersects the upper surface of the wing. From Figure 25, we can estimate that the time-averaged flow is separated for more than 40% of chord in the DES simulation and slightly less than 40% of the chord in the RANS simulations. The experimental data shows reattachment at approximately the 30% chord position. DES results show a secondary recirculation region indicated by the green color ahead of the 10% chord position. This secondary recirculation region is much less pronounced in the RANS results. Although the experimental data does not show a secondary recirculation region, it is likely that such a region does exist. Regardless, the DES result appears to overpredict the extent of this secondary flow.

Figure 26 shows a comparison of the separation and attachment lines in the predicted flow fields estimated using the critical point-based approach of Kenwright [33]. The attachment lines shown in Figure 26 are consistent with the positions estimated from Figure 25. As noted above, the velocity contours suggest a larger secondary recirculation region in the time-averaged DES computations. The broken red spanwise line, the separation line for the secondary recirculation, is shifted farther aft in the DES computations. In both cases, the blue reattachment line is located very near the horn. There is an anomalous reattachment near the trailing edge in the DES results, which is unexplained.

Figure 27 depicts a comparison between the RMS of the fluctuations in the streamwise velocity component predicted by the DES computation and experimental data. The turbulence intensity was calculated as the root-mean-square of the fluctuating x-component of velocity normalized by the freestream velocity. The fields are qualitatively similar, with the exception that the location of the maximum value of the fluctuation is shifted upward and the value is larger in magnitude in the predicted results.

Table 3: Comparison of predicted lift and drag coefficients and experimental data for the extruded wing (baseline mesh at 4° angle of attack with Δt=0.15ms)

	Lift Coefficient (C_L)	Drag Coefficient (C_D)
Experimental (α=4.129)	0.496	0.0568
Steady RANS results (baseline mesh)	0.430	0.0485
Time-averaged DES results (baseline mesh with Δt=0.15ms)	0.414	0.049

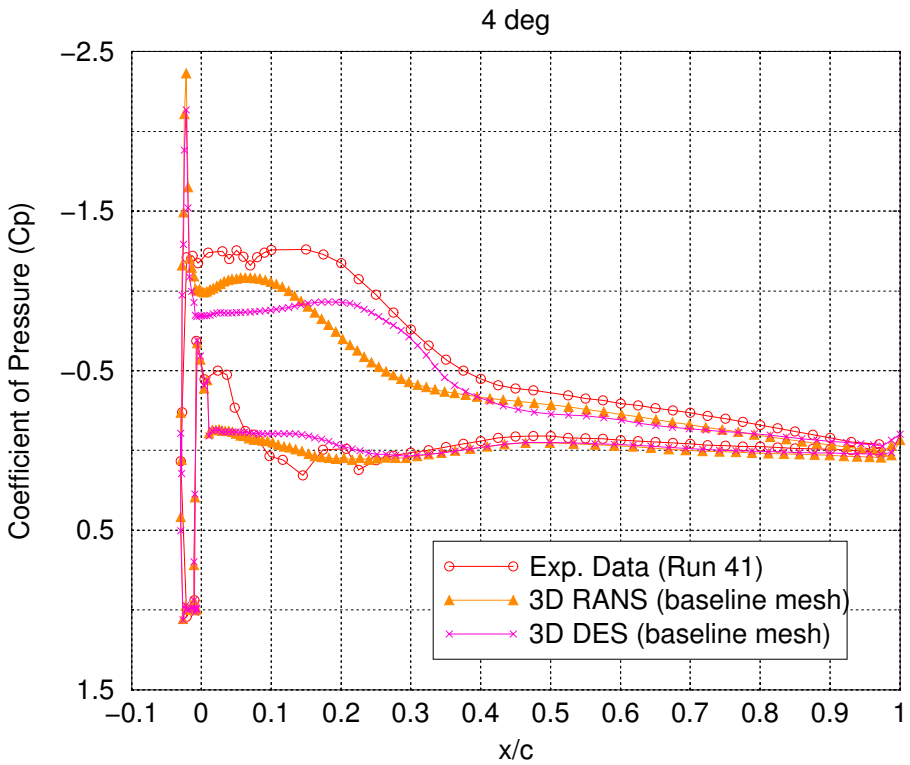

Figure 24: Comparison of predicted midspan wing pressure coefficients and experimental data for the extruded wing (baseline mesh at $4°$ angle of attack with Δt=0.15ms)

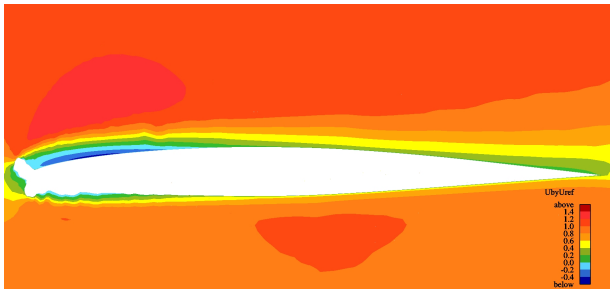

(a) Steady RANS results (baseline mesh)

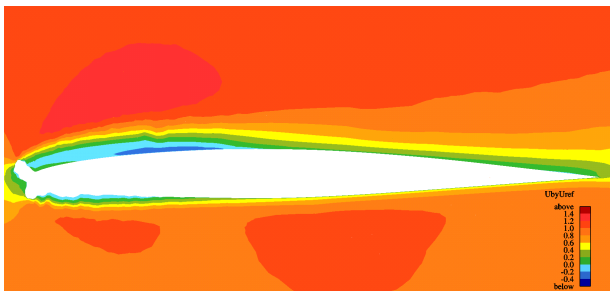

(b) Time-averaged DES results (baseline mesh with Δt=0.15ms)

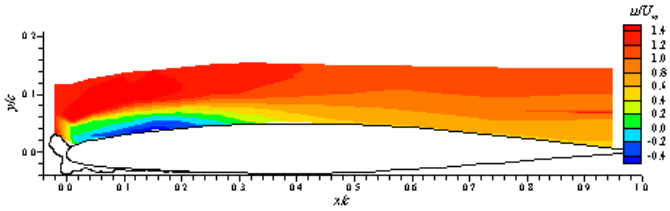

(c) Experimental hot-split-film data [18]

Figure 25: Comparison of predicted midspan u-velocity contours and experimental data for the extruded wing (baseline mesh at $4°$ angle of attack with Δt=0.15ms)

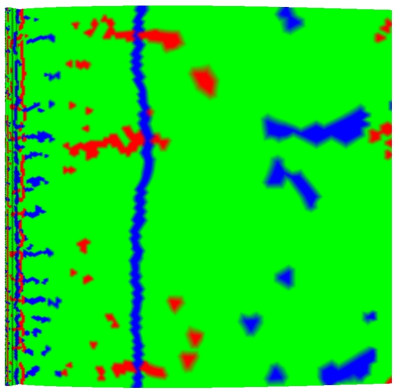

(a) Steady RANS results (baseline mesh)

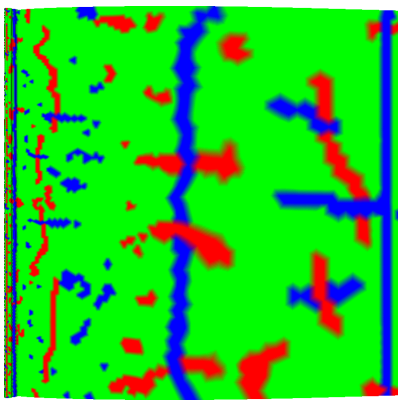

(b) Time-averaged DES results (baseline mesh with Δt=0.15ms)

Figure 26: Comparison of predicted separation (red) and attachment (blue) locations for the extruded wing (baseline mesh at 4° angle of attack with Δt=0.15ms)

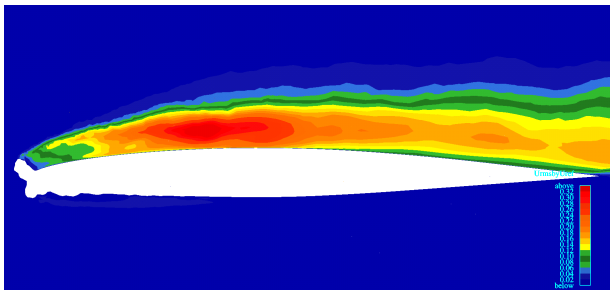

(a) DES results (baseline mesh at Δt=0.15ms)

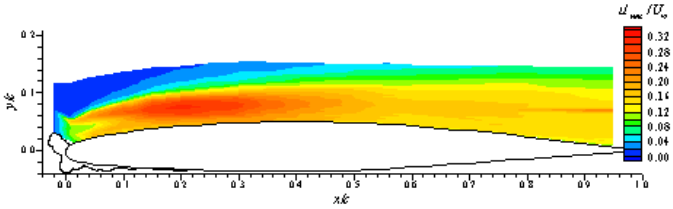

(b) Experimental hot-split-film data [18]

Figure 27: Comparison of the RMS of the fluctuations in the u-velocity component for the extruded wing (baseline mesh at 4° angle of attack with Δt=0.15ms)

4.3.3 Three-dimensional DES results: 6° angle of attack, Δt=0.15ms, baseline mesh

We now compare DES and RANS results computed using the baseline DES mesh with Δt=0.15ms with experimental data at 6° angle of attack. Table 4 shows a comparison of time-averaged lift and drag coefficients with corresponding RANS results and experimental data. Lift and drag coefficients from the DES computations compare well with the experimental data. However, as we will see below, the predicted flow field details do not show the level of agreement suggested by the lift and drag coefficients.

Figure 28 shows comparisons of predicted steady RANS and time-averaged DES midspan pressures with experimental data. The time-averaged DES results again suggest a large separation bubble centered just downstream of the midchord position. The predicted bubble position is aft of the position suggested by the experimental data. The pressure is seen to be relatively constant from leading edge to approximately 24% of the chord. Aft of this point, the pressure increases. The DES results show improved agreement with the experimental pressures in comparison to the RANS results. There are no significant differences between the DES results and RANS results on the lower surface. The improved agreement between the predicted force coefficients and the experimental data shown in Table 4 can be attributed at least in part to the strengthening of the recirculation on the wing upper surface relative to the RANS solution.

Figure 29 shows a comparison between the RANS results, the DES results, and the experimental data for the time-averaged x-component of the velocity at midspan. This figure shows that the time-averaged flow is separated over nearly the full chord for both the RANS and DES predictions, while the experimental data shows a reattachment at approximately 50% chord. As suggested by the pressure data, the time-averaged DES velocity data show that the recirculation is shifted aft, as indicated by the region darker blue color region. A secondary recirculation region, indicated by the green color adjacent to the wing ahead of the 15% chord position, is larger in the DES results than in the RANS results, which is consistent with the 4° angle of attack case.

Figure 30 shows a comparison of the separation and attachment lines in the predicted flow fields. The flow separates from the horn and reattaches at the trailing edge as indicated by the dark blue line across the span. These results are consistent with Figure 29. Velocity contours from Figure 29 suggest a larger secondary recirculation region in the time-averaged DES computations. The broken red spanwise line in Figure 30 seems to confirm this result.

Figure 31 depicts a comparison between the RMS of the fluctuations in the x-component of the velocity predicted by the DES computations and experimental data. The predicted region of maximum intensity is shifted upward and is conspicuously larger in extent than that shown in the experimental data. This suggests that the predicted unsteadiness is more pronounced than the physical unsteadiness. However, the region of green just downstream of the horn indicates smaller values of the fluctuating component. This implies that the secondary recirculation that exists in this region is fairly stable.

Figure 32 illustrates the unsteady, three-dimensional nature of the DES computation. Figure 32 shows isovorticity surfaces ($300s^{-1}$) colored by pressure at six different non-dimensional times. The total time interval shown in these figures is 0.75s. As can be seen from the images, the flow is highly unsteady and there is significant three-dimensionality in the flow once the vortex sheet begins to roll up. The low-pressure regions in the pressure field (blue in color) signify the presence of vortex cores.

Table 4: Comparison of predicted lift and drag coefficients and experimental data for the extruded wing (baseline mesh at 6° angle of attack with Δt=0.15ms)

	Lift Coefficient (C_L)	Drag Coefficient (C_D)
Experimental (α = 6.124)	0.659	0.105
Steady RANS results (baseline mesh)	0.561	0.083
Time-averaged DES results (baseline mesh with Δt=0.15ms)	0.656	0.098

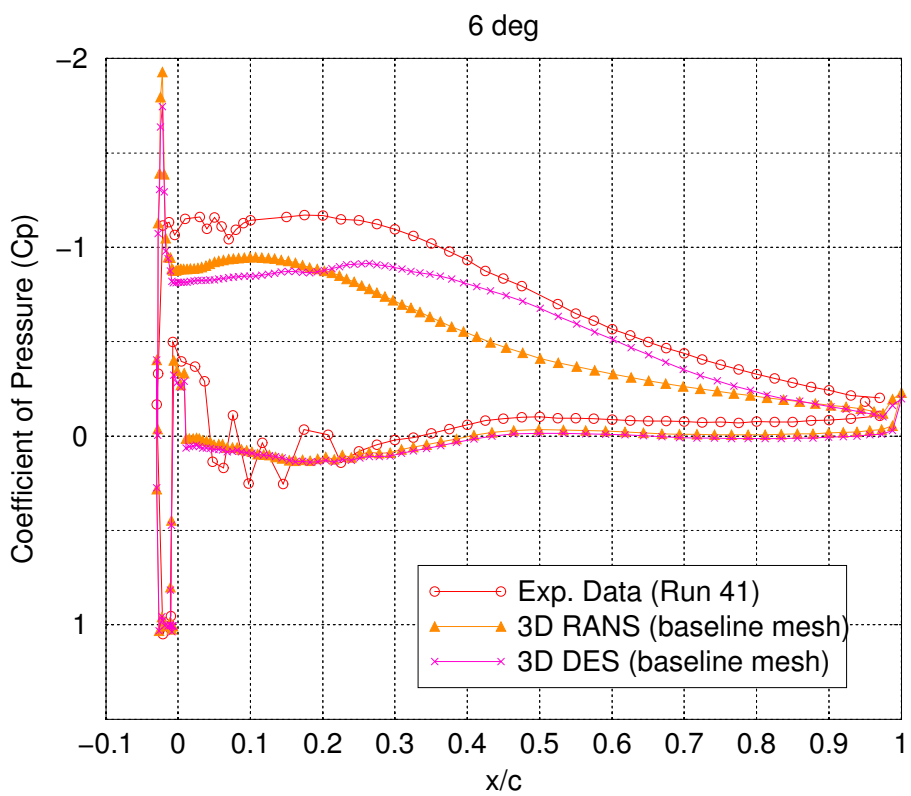

Figure 28: Comparison of predicted midspan wing pressure coefficients and experimental data for the extruded wing (baseline mesh at 6° angle of attack with Δt=0.15ms)

(a) Steady RANS results (baseline mesh)

(b) Time-averaged DES results (baseline mesh with Δt=0.15ms)

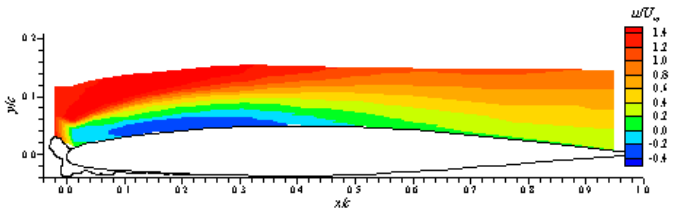

(c) Experimental hot-split-film data [18]

Figure 29: Comparison of predicted midspan u-velocity contours and experimental data for the extruded wing (baseline mesh at 6° angle of attack with Δt=0.15ms)

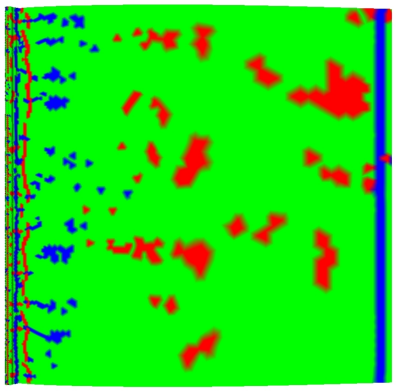

(a) Steady RANS results (baseline mesh)

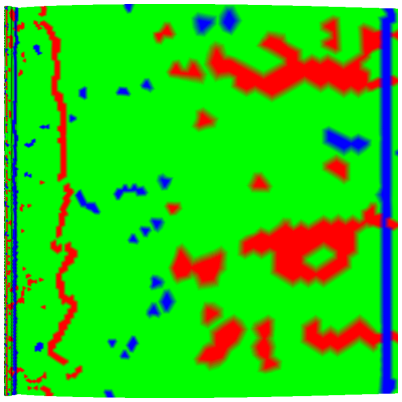

(b) Time-averaged DES results (baseline mesh with Δt=0.15ms)

Figure 30: Comparison of predicted separation (red) and attachment (blue) locations for the extruded wing (baseline mesh at 6° angle of attack with Δt=0.15ms)

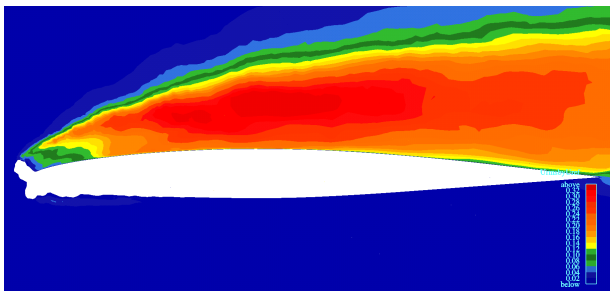

(a) DES results (baseline mesh with Δt=0.15ms)

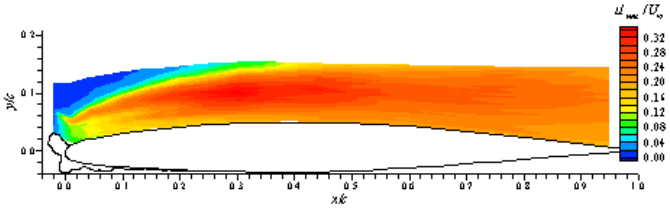

(b) Experimental hot-split-film data [18]

Figure 31: Comparison of the RMS of the fluctuations in the u-velocity component for the extruded wing (baseline mesh at 6° angle of attack with Δt=0.15ms)

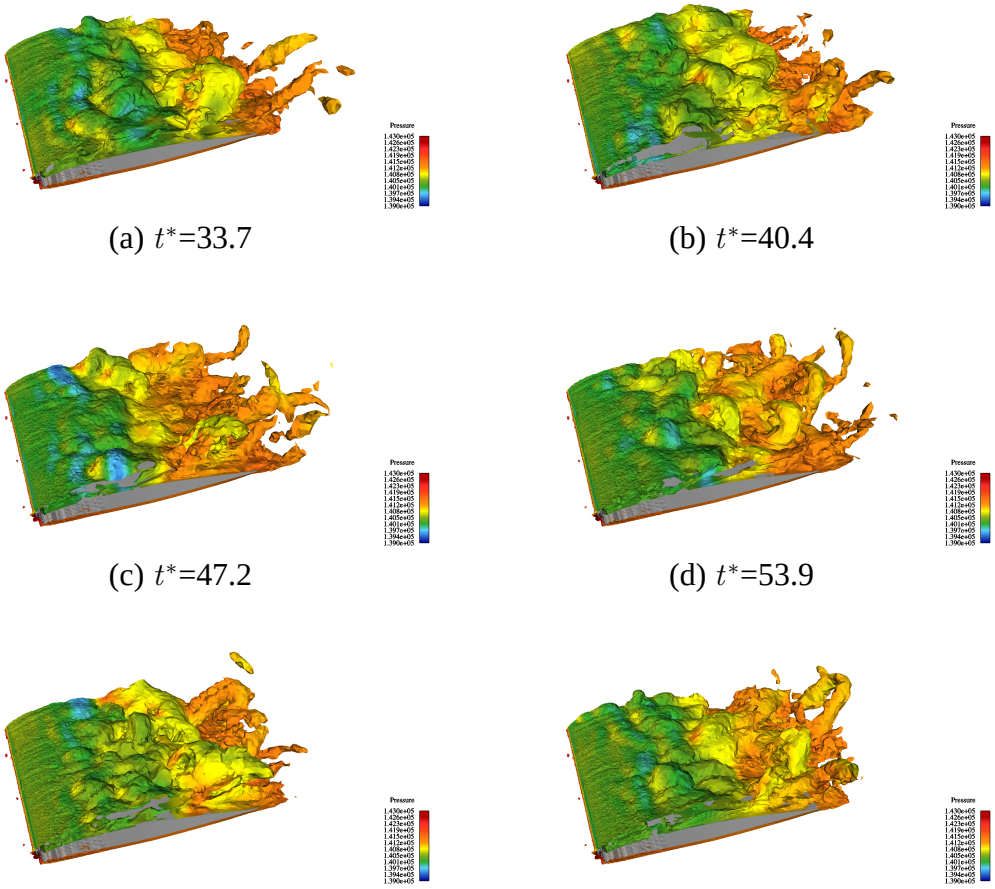

(a) t^*=33.7 (b) t^*=40.4

(c) t^*=47.2 (d) t^*=53.9

(e) t^*=60.7 (f) t^*=67.4

Figure 32: Isovorticity contours ($300s^{-1}$) colored by pressure for the DES baseline mesh at $6°$ angle of attack with Δt=0.15ms

4.3.4 Three-dimensional DES results: 6° angle of attack, Δt=0.075ms, baseline mesh

In this section, results obtained using the three-dimensional baseline DES mesh with Δt=0.075ms are compared with RANS results and experimental data for a 6° angle of attack. Table 5 shows a comparison of time-averaged lift and drag coefficients with the corresponding RANS solutions and the experimental data. In general, the lift and drag coefficients compare well with experimental data.

Figure 33 shows comparisons of predicted time-averaged midspan pressures with experimental data. Overall, the time-averaged DES results at Δt=0.075ms are quite similar to the Δt=0.15ms results. As before, the agreement between the predicted DES results and the experimental data is not commensurate with that suggested by the lift and drag data. Figures 34 and 35 compare the time-averaged x-component of the velocity at midspan and the separation and attachment lines in the predicted flow fields. Again, the extent of the separated region is overpredicted. The separation and attachment line images are consistent with the velocity contours. Figures 34 and 35 again suggest the presence of a significant secondary recirculation region. Figure 36 compares the predicted turbulence intensities with experimental data. This image shows that the intensity of the fluctuations is increased in the predictions and occurs over a larger region than in the experimental data. The stability of the secondary flow structure is again evident.

Figure 37 shows isovorticity surfaces ($300s^{-1}$) colored by pressure at six different non-dimensional times. The total time lapse shown in these figures is, again, 0.75s. The low-pressure regions in the pressure field (blue in color) indicate the presence of vortex cores. These images indicate that the flow field is highly unsteady and three dimensional.

Table 5: Comparison of predicted lift and drag coefficients and experimental data for the extruded wing (baseline mesh at 6° angle of attack with Δt=0.075ms)

	Lift Coefficient (C_L)	Drag Coefficient (C_D)
Experimental (α = 6.124)	0.659	0.105
Steady RANS results (baseline mesh)	0.561	0.083
Time-averaged DES results (baseline mesh with Δt=0.075ms)	0.677	0.098

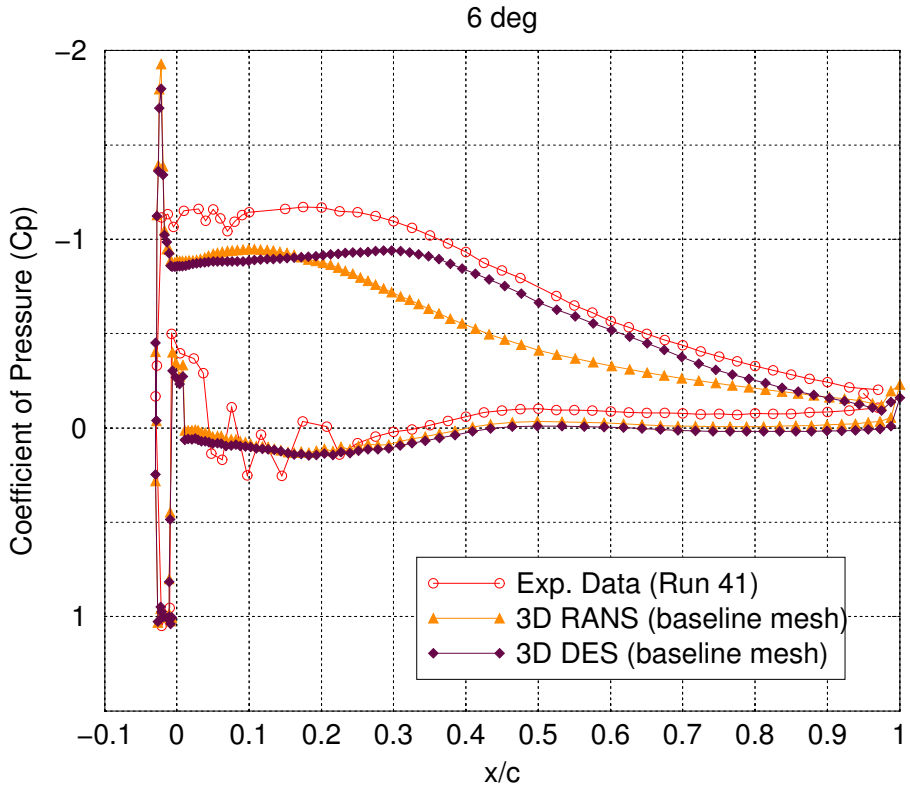

Figure 33: Comparison of predicted midspan wing pressure coefficients and experimental data for the extruded wing (baseline mesh at $6°$ angle of attack with Δt=0.075ms)

(a) Steady RANS results (baseline mesh)

(b) Time-averaged DES results (baseline mesh with Δt=0.075ms)

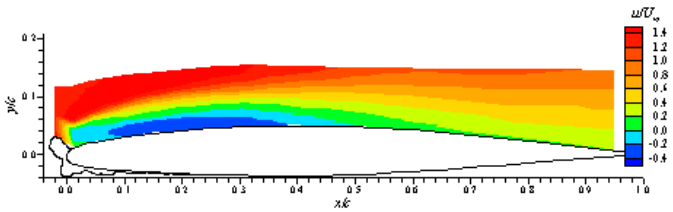

(c) Experimental hot-split-film data [18]

Figure 34: Comparison of predicted midspan u-velocity contours and experimental data for the extruded wing (baseline mesh at 6° angle of attack with Δt=0.075ms)

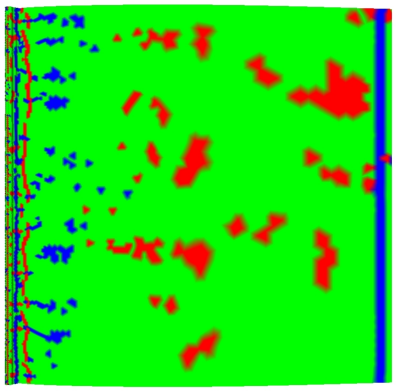

(a) Steady RANS results (baseline mesh)

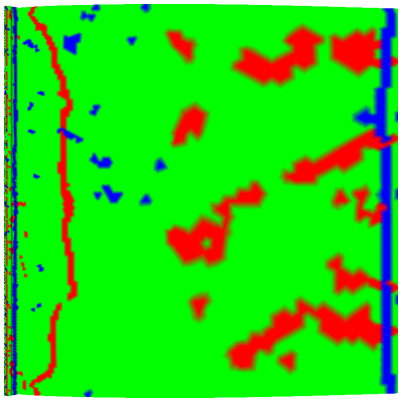

(b) Time-averaged DES results (baseline mesh with Δt = 0.075ms)

Figure 35: Comparison of predicted separation (red) and attachment (blue) locations for the extruded wing (baseline mesh at 6° angle of attack with Δt=0.075ms)

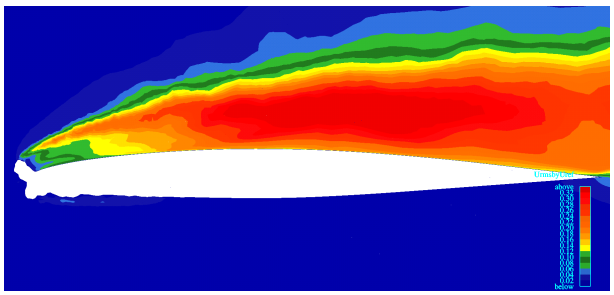

(a) DES results (baseline mesh with Δt=0.075ms)

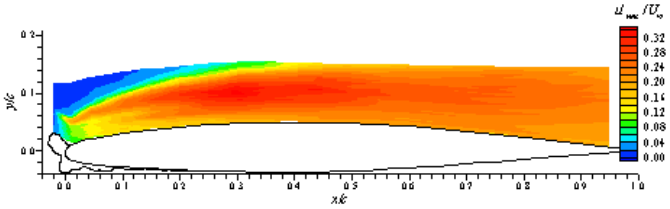

(b) Experimental hot-split-film data [18]

Figure 36: Comparison of the RMS of the fluctuations in the u-velocity component for the extruded wing (baseline mesh at 6° angle of attack with Δt=0.075ms)

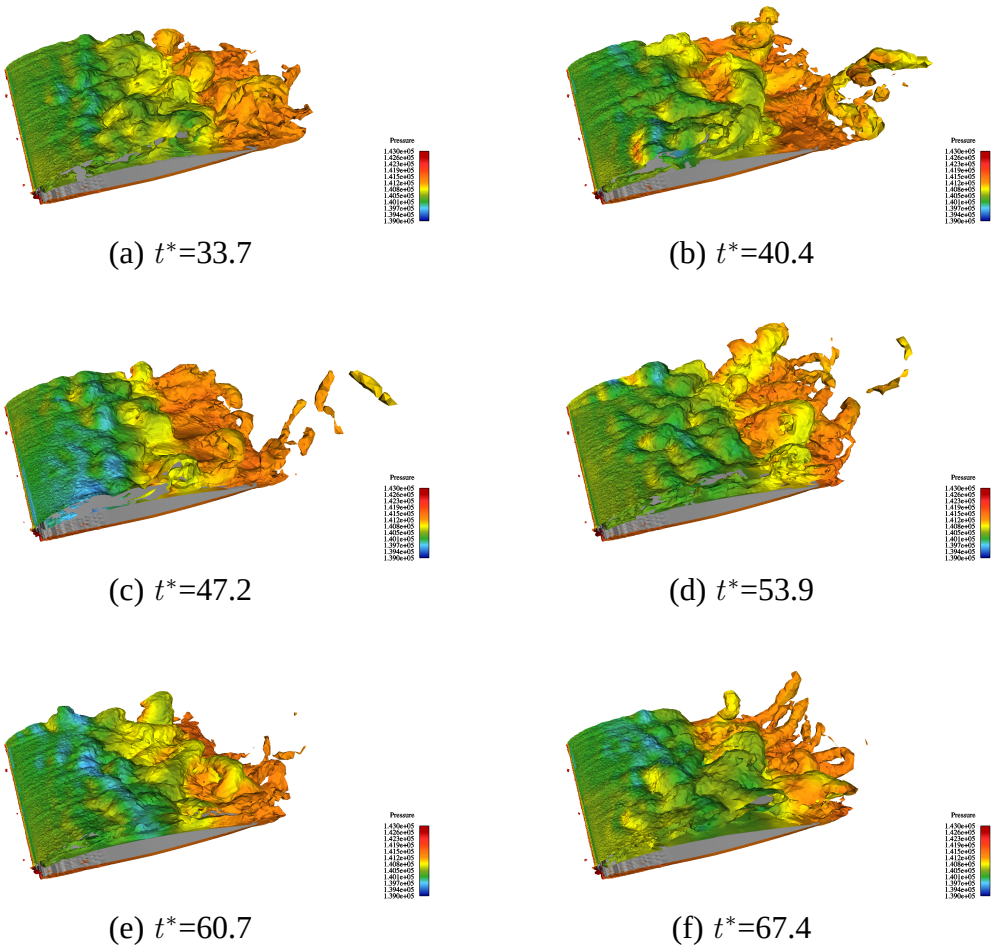

(a) t^*=33.7 (b) t^*=40.4

(c) t^*=47.2 (d) t^*=53.9

(e) t^*=60.7 (f) t^*=67.4

Figure 37: Isovorticity contours ($300s^{-1}$) colored by pressure for the DES baseline mesh at $6°$ angle of attack with Δt=0.075ms

4.3.5 Three-dimensional DES results: 6° angle of attack, Δt=0.075ms, refined mesh

In this section, DES results obtained using the refined DES mesh with Δt=0.075ms are compared steady RANS results and experimental data for a 6° angle of attack. Table 6 shows a comparison of time-averaged lift and drag coefficients with the corresponding RANS results and experimental data. The lift and drag coefficients again compare well with the experimental data.

Figure 38 shows that the constant pressure region terminates around $x/c \approx 0.28$. Even in this case, the extent of separation bubble is overpredicted when compared to experimental data. The lower surface pressure distribution is similar for the RANS and DES results. Figure 39 shows comparisons between predicted time-averaged x-component of the velocity at midspan and experimental data. From this figure we can note that even though the separation region extends up to the trailing edge, the intensity of the reverse flow is decreased as the boundary layer reattaches. This is evident in the decrease of the blue region near the trailing edge. The secondary recirculation region is again evident. Separation and reattachment lines from Figure 40 indicate flow features consistent with those shown in Figure 39.

The turbulence intensity contours for the extruded wing in Figure 41 agree qualitatively with the corresponding experimental data. Here the location of maximum intensity is shifted slightly upward and to the right. Isovorticity surfaces ($300s^{-1}$) colored by pressure at six different non-dimensional times are shown in Figure 42. Here, the vortex cores are more readily discerned than in the other results. The improved spatial resolution is most likely responsible for this result.

Table 6: Comparison of predicted lift and drag coefficients and experimental data for the extruded wing (refined mesh at 6° angle of attack with Δt=0.075ms)

	Lift Coefficient (C_L)	Drag Coefficient (C_D)
Experimental (α=6.124)	0.659	0.105
Steady RANS results (refined mesh)	0.558	0.085
Time-averaged DES results (refined mesh with Δt=0.075ms)	0.666	0.090

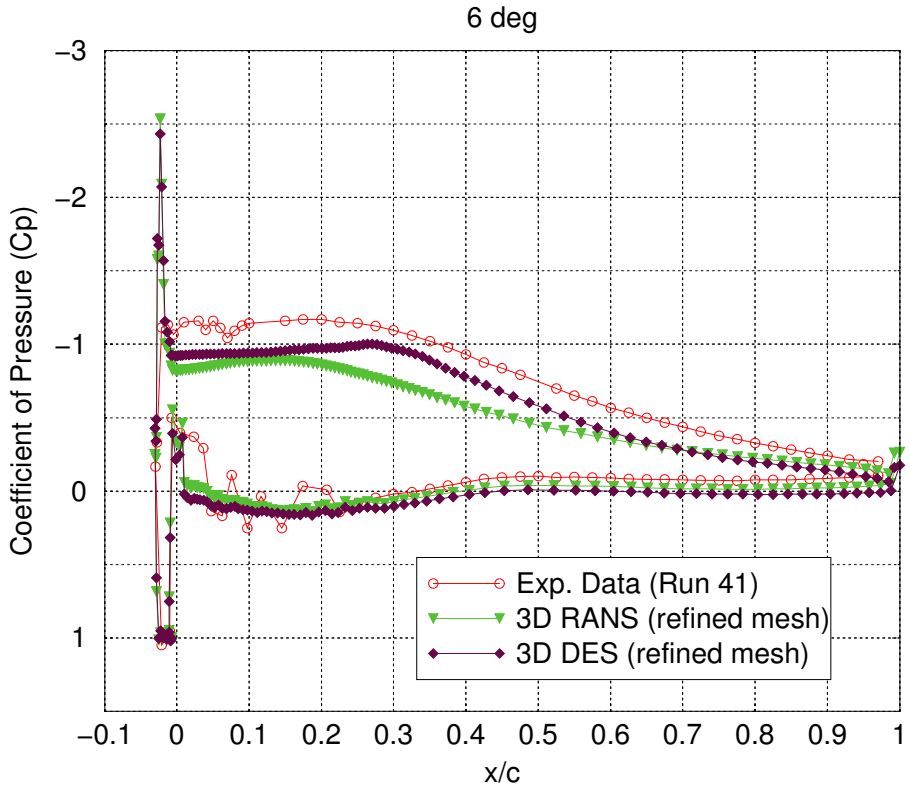

Figure 38: Comparison of predicted midspan wing pressure coefficients and experimental data for the extruded wing (refined mesh at $6°$ angle of attack with Δt=0.075ms)

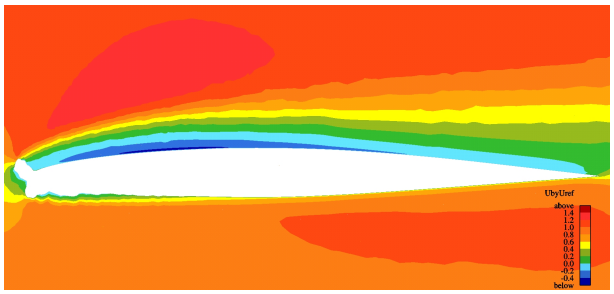

(a) Steady RANS results (refined mesh)

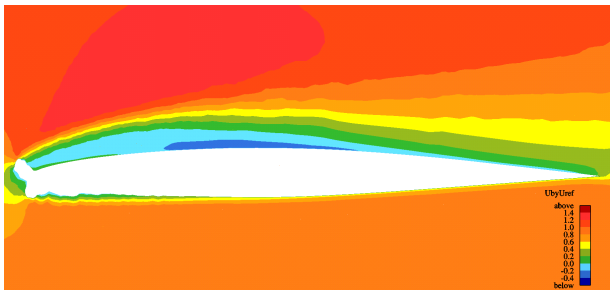

(b) Time-averaged DES results (refined mesh with Δt=0.075ms)

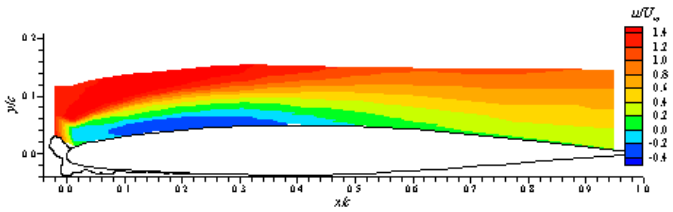

(c) Experimental hot-split-film data [18]

Figure 39: Comparison of predicted midspan u-velocity contours and experimental data for the extruded wing (refined mesh at 6° angle of attack with Δt=0.075ms)

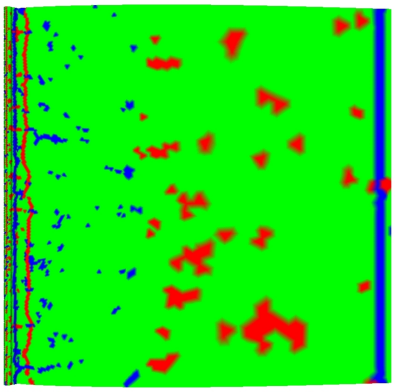

(a) Steady RANS results (refined mesh)

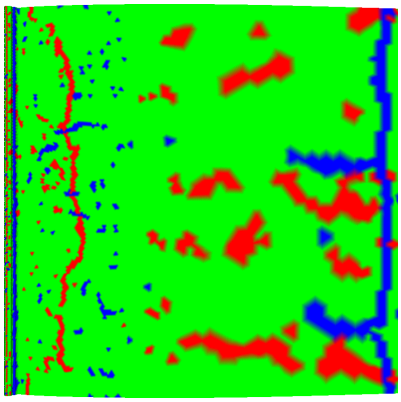

(b) Time-averaged DES results (refined mesh with Δt=0.075ms)

Figure 40: Comparison of predicted separation (red) and attachment (blue) locations for the extruded wing (refined mesh at 6° angle of attack with Δt=0.075ms)

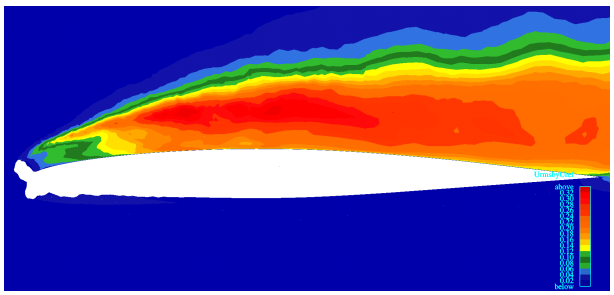

(a) DES results (refined mesh with Δt=0.075ms)

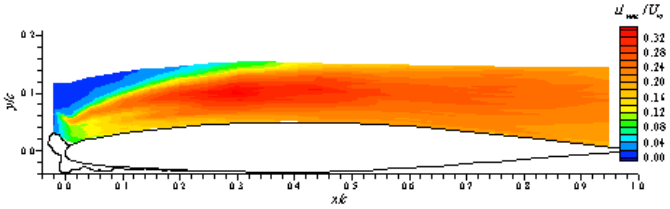

(b) Experimental hot-split-film data [18]

Figure 41: Comparison of the RMS of the fluctuations in the u-velocity component for the extruded wing (refined mesh at 6° angle of attack with Δt=0.075ms)

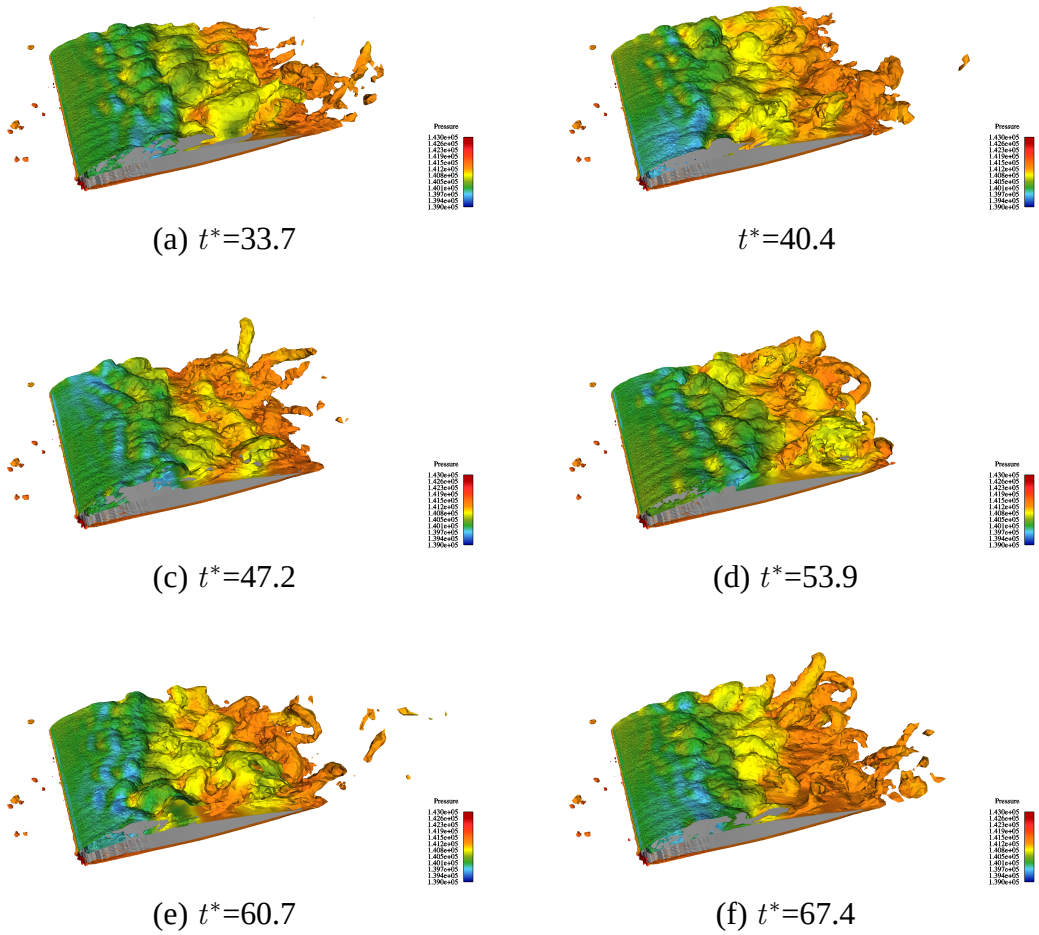

(a) t^*=33.7 t^*=40.4

(c) t^*=47.2 (d) t^*=53.9

(e) t^*=60.7 (f) t^*=67.4

Figure 42: Isovorticity contours ($300s^{-1}$) colored by pressure at $6°$ angle of attack with Δt=0.075ms

4.3.6 Mesh refinement and time step refinement comparisons

This section summarizes the effects of mesh refinement and timestep refinement for three-dimensional DES computations. Table 7 and Figures 43(a) and 43(b) show comparisons of force coefficients from steady RANS and DES solutions. In general, we can see that there is no significant improvement in the accuracy of the solution after mesh refinement. There is some improvement in the lift prediction for the DES solution for the 4° angle of attack case with time step refinement. Figure 44 shows comparisons of the predicted time-averaged, three-dimensional midspan pressure coefficients for the extruded wing with experimental data using the baseline mesh and the refined mesh at an angle of attack of 6°. From the figure and Table 7, we can note that mesh refinement and time-step refinement do not significantly improve the accuracy in the solution when compared to the experimental data. This suggests that the baseline mesh with Δt=0.15ms, as estimated from the guidelines given by Spalart [7], is sufficient for this case. The above conclusion is further supported by the streamwise velocity component images (Figures 29, 34 and 39), separation and attachment line images (Figures 30, 35 and 40), and turbulence intensity images (Figures 31, 36 and 41).

The isovorticity contour images (Figures 32, 37 and 42) confirm that there is significant three-dimensionality in the flow. As the timestep and mesh are refined, we also note that the intensity of the reverse flow is decreased as the boundary layer reattaches. This is evident from Figures 34 and 39 through a decrease in the extent of the blue region near the trailing edge. The turbulence intensity for the refined mesh with Δt=0.075ms at a 6° angle of attack compares better with the corresponding experimental data. This can be seen from Figure 41.

To validate the three-dimensional DES solutions obtained for the baseline and refined meshes, the periodogram function of MATLAB [34] was used to analyze the time histories of the wing lift coefficient. Figure 45 shows the lift force history for the refined mesh with Δt=0.075ms at a 6° angle of attack. Figure 45(a) shows the lift history for both RANS and DES computations, whereas Figure 45(b) shows only the lift history for the DES computation. It is representative of the other simulations. The power spectral density (PSD) of the time history of the lift coefficient is computed and plotted against the frequency of the signal. The time interval was 0.75s to 1.5s after the initiation of the DES computation. For Δt=0.075ms, this corresponds to 10,000 time steps. For Δt=0.15ms, this corresponds to 5,000 time steps.

Figure 46 shows a comparison of the PSD signatures for the three-dimensional DES solutions on the baseline and refined meshes with Δt=0.075ms for 6° angle of attack. From the figure, it is apparent that similar signatures are obtained up to 15Hz. Figure 46(b), which is the zoomed version of Figure 46(a) in the frequency range 10-100Hz, shows differences above 15Hz. Figure 47 shows a comparison of three-dimensional DES solution on baseline mesh with Δt=0.15ms and Δt=0.075ms for 6° angle of attack. Again, Figure 47 shows very similar signatures up to 10Hz. Figure 47(b), which is the zoomed version of Figure 47(a) in the frequency range of 10-100Hz, again shows there are some quantitative differences at frequencies of approximately 12Hz.

These results indicate that both the time-step refinement and mesh refinement only significantly affected the signal at frequencies higher than 12-15Hz. The power at these frequencies is at least an order of magnitude less (range 10^{-04} to 10^{-06}) than the power at the lower frequencies. Taken together with the fact that the time-averaged quantities are so similar, we can conclude that these refinements did not significantly affect the results of the simulations. Since the character of the solutions did not change with these refinements, this suggests that we have valid DES results within the context of the AVUS flow solver. This does not address the accuracy of the simulation.

Table 7: Comparison of lift and drag coefficients for all three-dimensional RANS and DES results (coarse RANS mesh, baseline DES mesh and refined DES mesh)

	C_L			
Angle of Attack (α)	0	2	4	6
Experimental (α)	-0.024	2.1	4.129	6.124
Experimental	0.063	0.289	0.496	0.660
3D-RANS (Coarse)	0.065	0.265	0.443	0.556
3D-RANS (Baseline)	0.065	0.251	0.430	0.561
3D-RANS (Refined)	0.066	0.254	0.438	0.558
3D-DES (Baseline, Δt=0.15ms)	N/A	N/A	0.414	0.656
3D-DES (Baseline, Δt=0.075ms)	N/A	N/A	0.438	0.670
3D-DES (Refined, Δt=0.075ms)	N/A	N/A	0.445	0.660

	C_D			
Angle of Attack (α)	0	2	4	6
Experimental (α)	-0.024	2.1	4.129	6.124
Experimental	0.042	0.041	0.076	0.105
3D-RANS (Coarse)	0.039	0.042	0.059	0.098
3D-RANS (Baseline)	0.036	0.037	0.048	0.083
3D-RANS (Refined)	0.035	0.035	0.048	0.085
3D-DES (Baseline, Δt=0.15ms)	N/A	N/A	0.049	0.098
3D-DES (Baseline, Δt=0.075ms)	N/A	N/A	0.050	0.098
3D-DES (Refined, Δt=0.075ms)	N/A	N/A	0.047	0.090

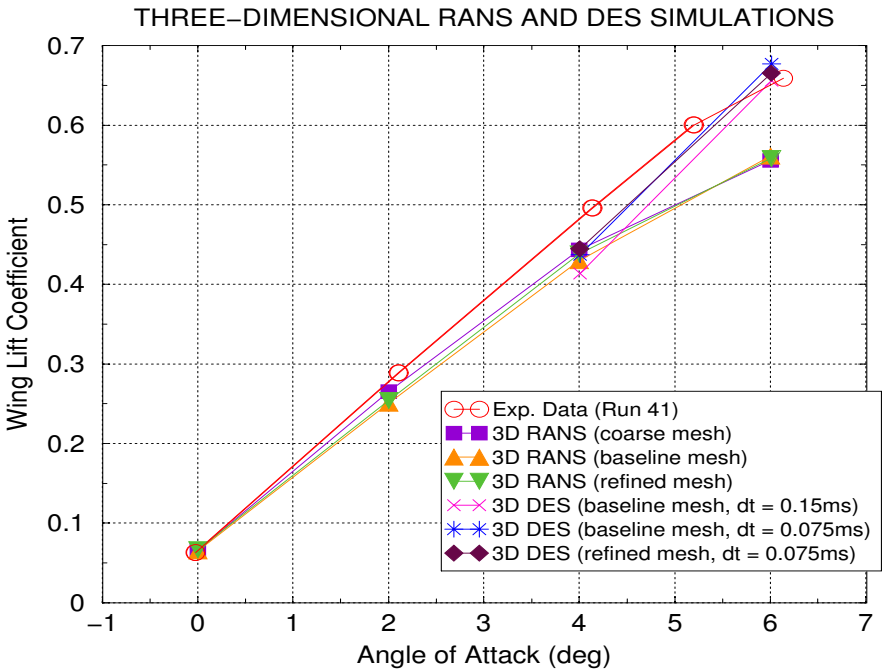

(a) Lift coefficients

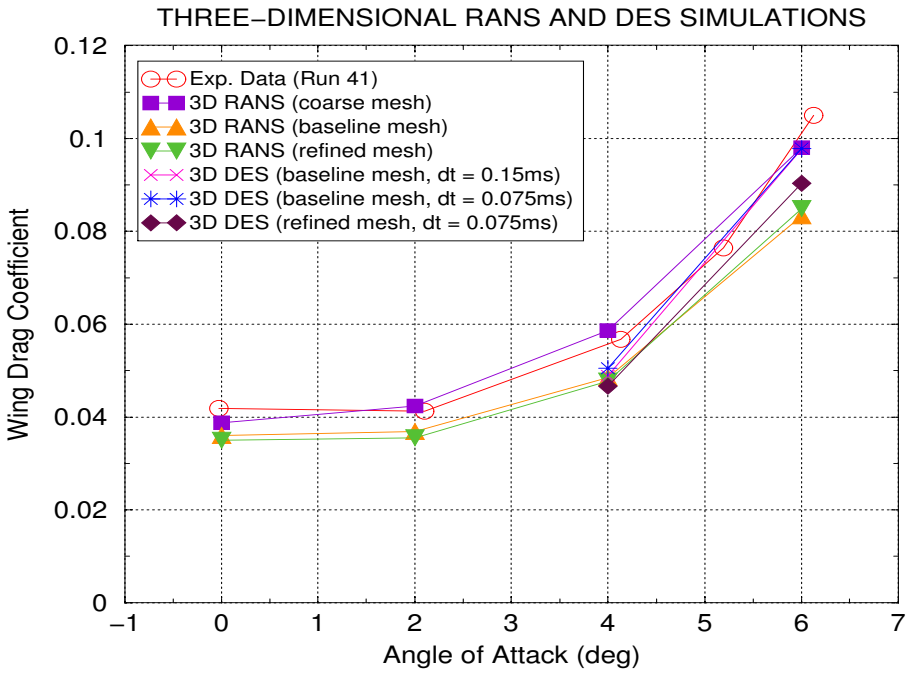

(b) Drag coefficients

Figure 43: Comparison of predicted wing lift and drag coefficients and experimental data for the extruded wing (coarse RANS mesh, baseline DES mesh and refined DES mesh)

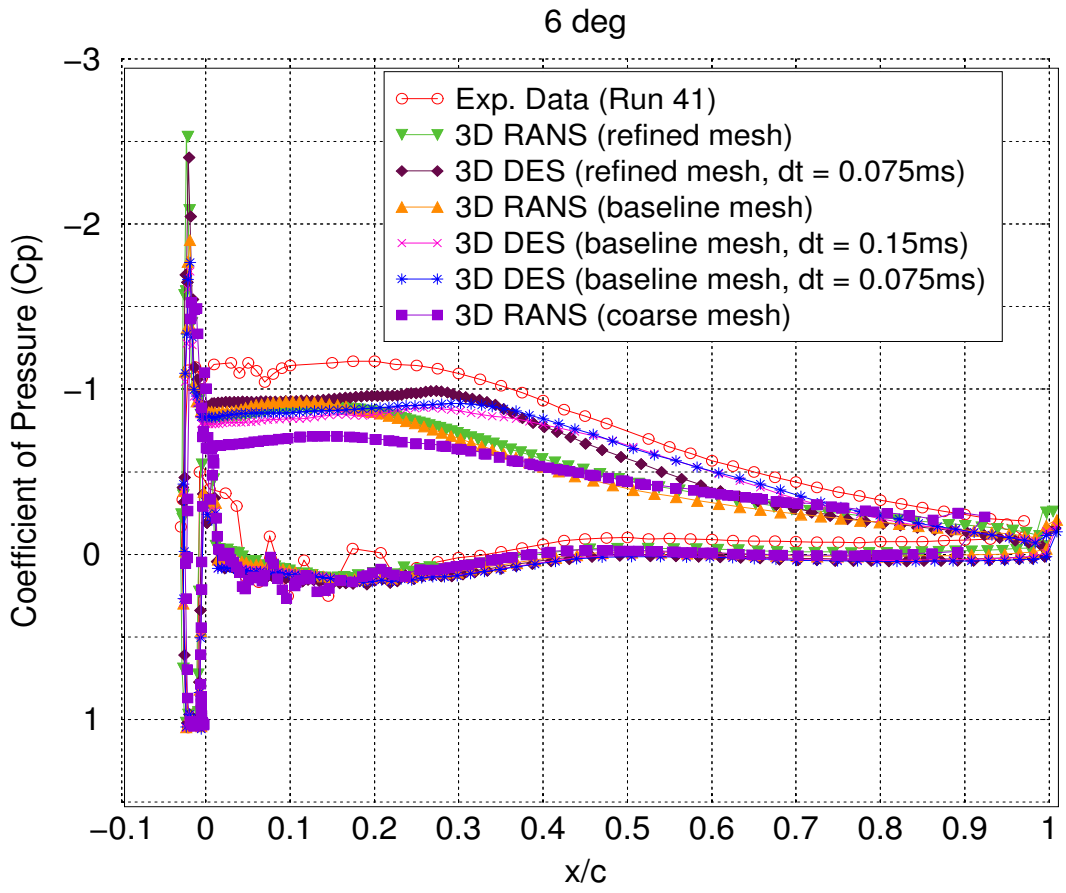

Figure 44: Comparison of predicted midspan wing pressure coefficients and experimental data for the extruded wing (coarse RANS mesh, baseline DES mesh and refined DES mesh at 6° angle of attack)

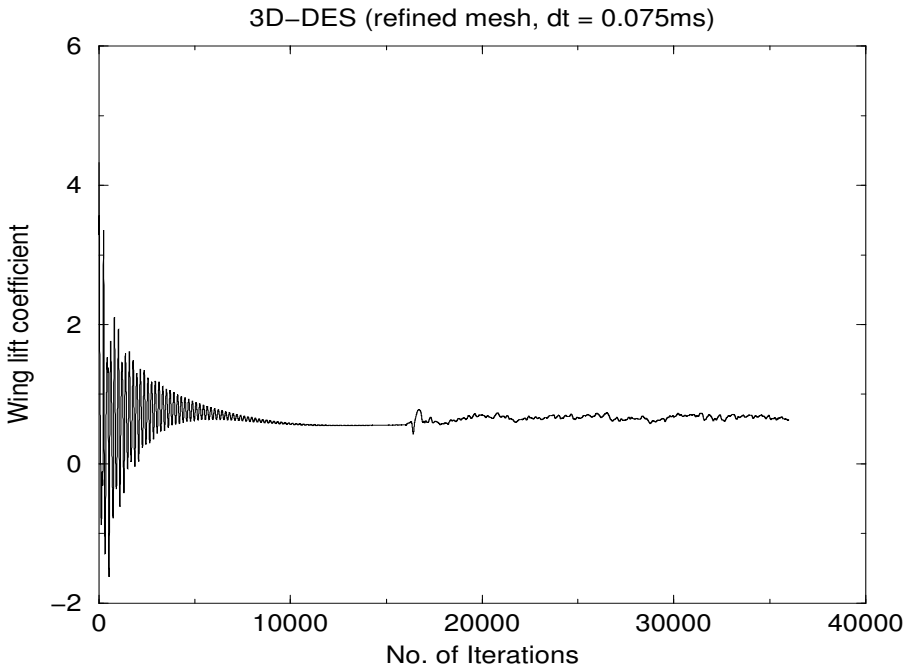

(a) Lift history for RANS and DES computations

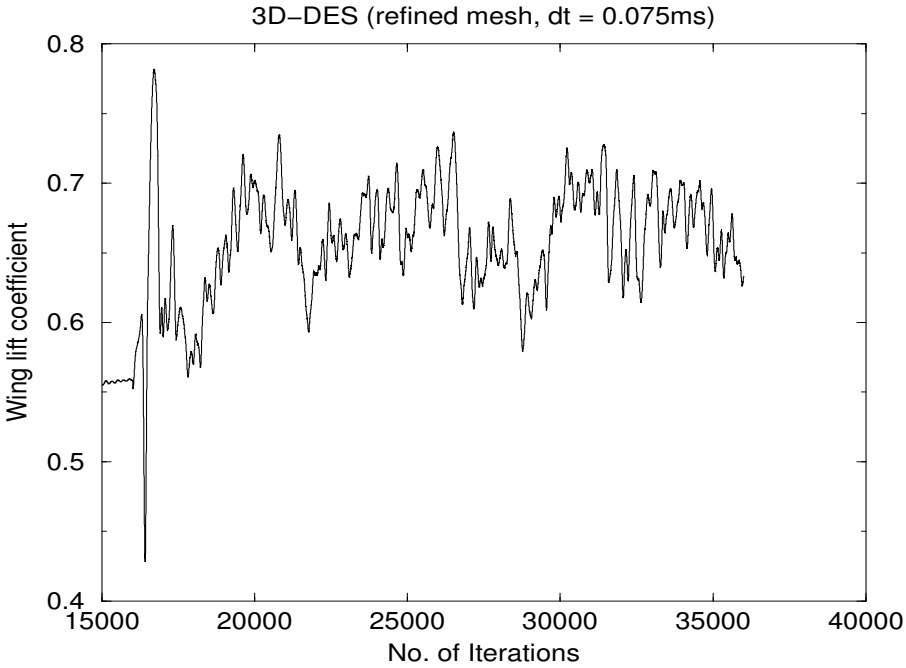

(b) Zoomed version of Figure 45(a) showing DES lift history

Figure 45: Lift history for refined mesh with Δt=0.075ms

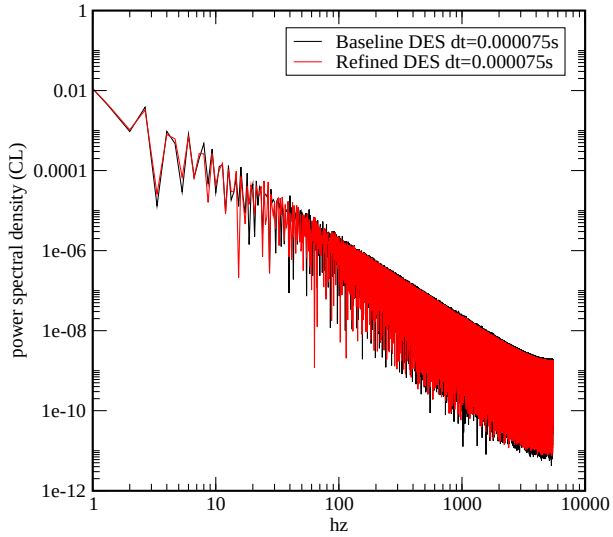

(a) Power spectral density

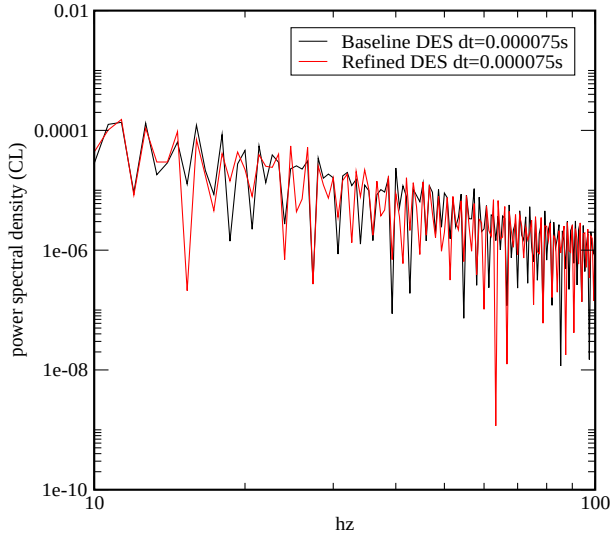

(b) Power spectral density (zoomed version of Figure 46(a)

Figure 46: Comparison of power spectral density plots for baseline mesh and refined mesh at $6°$ angle of attack, with Δt=0.075ms

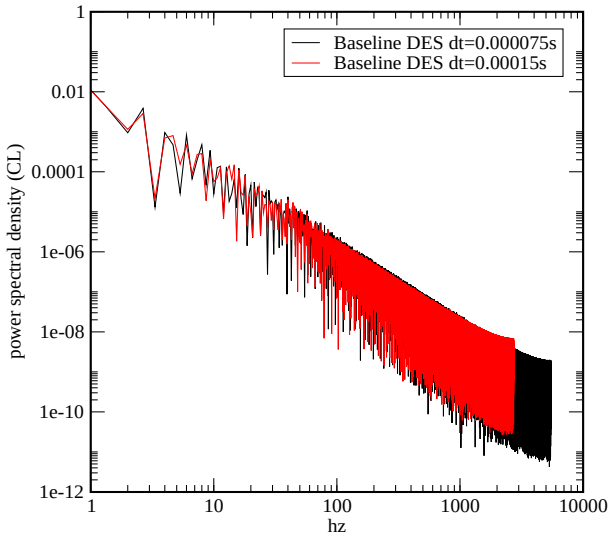

(a) Power spectral density

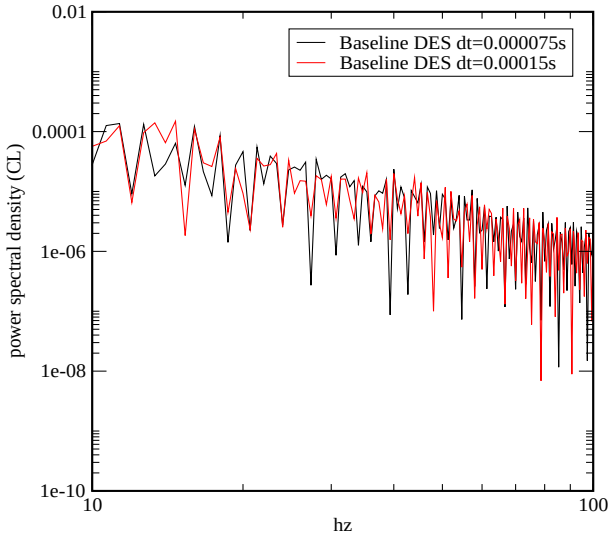

(b) Power spectral density (zoomed version of Figure 47(a)

Figure 47: Comparison of power spectral density plots for baseline mesh at 6° angle of attack with, Δt=0.15ms and Δt=0.075ms

5. Assessment of Existing Capabilities and Recommendations

In this section, we provide an assessment of the technologies employed in this effort and make a few recommendations regarding potential roles they may play in icing effects analysis.

5.1 Tool assessment

1. The mesh generation tools employed here performed adequately for the iced wing problem. SolidMesh proved somewhat difficult to use due to the fact that control of point spacing in the interior of the domain was challenging. The source-based approach employed in the GridTool/VGridns combination provided an effective mechanism to control the point spacing in the domain. However, we did encounter some difficulties generating a complete mesh. These problems were solved by trial-and-error adjustment of the source strengths.

2. Effective utilization of the AVUS flow solver was challenging because we were unable to consistently execute the program on more than 64 processors. Considering the time required to obtain DES solutions, this represents a significant impediment to routine deployment of the flow solver for DES computations – *even if sufficient resources were available*. Additionally, while analysis of the results indicates that the DES solutions are valid, questions remain about the quality of the solution. In particular, if additional resolution is required near the horn, it may make the computation cost prohibitive.

5.2 Recommendations

1. For constant section unswept wings, results obtained here suggest that there is no need to employ three-dimensional steady RANS simulations. Although there is some three-dimensional flow present in the solutions, it seems to have little influence. Additionally, the steady three-dimensional RANS simulations do not model the three-dimensionality present in the unsteady DES computations. Two-dimensional steady RANS computations appear to be adequate for configurations of this type.

2. Conversely, there is no compelling reason to employ two-dimensional DES computations. As reported here and elsewhere [12], the two-dimensional DES computations significantly overpredict the effects of the unsteady flow field. This is an inherent limitation of the two-dimensional approximation.

3. It is our opinion that DES should continue to be investigated for application to the icing effects problem. Other cases should be simulated so that a better assessment of DES capabilities may be obtained. However, the results observed here indicate that only configurations for which detailed experimental flow field data is available should be considered.

4. It is also our opinion that, due to the significant unsteadiness observed in the experimental results [35], the extruded GLC305/944-ice shape may represent a particularly difficult case. Therefore, computations should be performed for configurations with less challenging horn ice accretions. Because of the detailed LDV measurements, one candidate configuration is the swept wing with simulated ice studied by Bragg, et al. [36, 37].

5. Because we believe that the hybrid RANS/LES strategy is the best near-term option for computing these complex flow fields, other hybrid RANS/LES implementations should be investigated along with other flow solvers to address questions about AVUS-specific behaviors.

6. Summary

The problem of flow field simulation for iced wing configurations is a complex one that severely taxes existing capabilities for geometry modeling, mesh generation, and flow solution. In this report, we focused on activities associated with the first year of an effort to investigate the capability of existing flow simulation methodologies to predict the separated, highly unsteady flow fields associated with wings with significant horn-ice accretions. The effectiveness of Detached-Eddy Simulation (DES) as a tool for predicting icing effects was evaluated. The AVUS code was employed to compute solutions for an iced wing configuration using DES and steady Reynolds Averaged Navier-Stokes (RANS) equation methodologies. The configuration was an extruded GLC305/944-ice shape section with a rectangular planform. The model was mounted between two walls so no tip effects were considered. The numerical results were validated by comparison with experimental data for the same configuration.

We presented the results of three-dimensional steady RANS computations and two- and three-dimensional DES computations performed for the extruded wing. The time-averaged DES computations showed improvement in lift and drag results near stall when compared to steady RANS results. However, flow field details did not show the level of agreement suggested by the integrated quantities.

The benefits of employing three-dimensional DES computations are not clear at this time. While comparisons of integrated time-averaged quantities such as lift and drag with experimental data are improved relative to steady RANS predictions, commensurate agreement was not obtained for detailed flow field quantities. In particular, DES results showed more extensive flow separation than the experimental data. Further, the DES results showed a significant secondary recirculation that was not present in the experimental data.

Based on our results, we believe that DES may prove useful in a limited sense to provide analysis of iced wing configurations when there is significant flow separation, e.g., near stall, where steady RANS computations are demonstrably ineffective. Additionally, we believe that DES may prove useful for flow fields with extensive three-dimensionality such as swept finite wings or wings with genuinely three-dimensional ice accretions. However, more validation is needed to determine what role DES can play as part of an overall icing effects prediction strategy.

References

[1] M. B. Bragg, A. P. Broeren, and L. A. Blumenthal. Iced-airfoil and wing aerodynamics. *SAE*, June 2003.

[2] I. Tani. *Low Speed Flows Involving Bubble Separations*. Pergamon, New York, 1964.

[3] M. Potapczuk. Numerical analysis of an NACA0012 airfoil with leading edge ice accretions, 1987. AIAA Paper 87-0101.

[4] J. Chung, Y. Choo, A. Reehorst, M. Potapczuk, and J. Slater. Navier-Stokes analysis of the flowfield characteristics of an ice contaminated aircraft wing, 1999. AIAA Paper 1999-0375.

[5] T. A. Dunn and E. Loth. Effects of simulated-spanwise-ice shapes on airfoils: Computational investigation, 1999. AIAA Paper 1999-0093.

[6] J. Pan, E. Loth, and M. B. Bragg. RANS simulations of airfoils with ice shapes, 2003. AIAA Paper 2003-0729.

[7] P. R. Spalart. Young-persons guide to detached-eddy simulation grids. Technical Report NASA CR-2001-211032, NASA, July 2001.

[8] P. R. Spalart, W. H. Jou, M. Strelets, and S. R. Allmaras. Comments on the feasibility of LES for wings, and on a hybrid RANS/LES approach. In *Advances in DNS/LES, 1st AFOSR International Conference on DNS/LES*, August 1997.

[9] J. R. Forsythe, K. D. Squires, K. E. Wurtzler, and P. R. Spalart. Detached-eddy simulation of fighter aircraft at high alpha, 2002. AIAA Paper 2002-0591.

[10] S. A. Morton, J. R. Forsythe, K. D. Squires, and K. E. Wurtzler. Assessment of unstructured grids for detached eddy simulation of high reynolds number separated flows. In *Proceedings of the 8th International Conference on Numerical Grid Generation in Computational Field Simulations*, Honolulu, June 2002.

[11] K. D. Squires, J. R. Forsythe, S. A. Morton, W. Z. Strang, K. E. Wurtzler, R. F. Tomaro, M. J. Grismer, and P. R. Spalart. Progress on detached-eddy simulation of massively separated flows, 2002. AIAA Paper 2002-102.

[12] S. Kumar and E. Loth. Detached-eddy simulations of an iced-airfoil, 2001. AIAA Paper 2001-0678.

[13] J. Pan and E. Loth. Detached-eddy simulations for airfoil with ice shapes, 2004. AIAA Paper 2004-0564.

[14] D. Thompson, S. Chalasani, and P. Mogili. Icing effects studies for a three-dimensional wing: Final report (NAG3-2562). Technical report, NASA GRC, May 2003.

[15] D. Thompson, P. Mogili, S. Chalasani, H. Addy, and Y. Choo. A computational icing effects study for a three-dimensional wing: Comparison with experimental data and investigation of spanwise variation, 2004. AIAA Paper 2004-056.

[16] H. Addy. Ice accretions and icing effects for modern airfoils. Technical Report NASA TP-2000-210031, NASA, April 2000.

[17] H. Addy, J. Zoeckler, and A. Broeren. A wind tunnel study of icing effects on a business jet airfoil, 2003. AIAA Paper 2003-0727.

[18] A. Broeren, H. E. Addy, and M. B. Bragg. Flowfield measurements about an airfoil with leading-edge ice shapes, 2004. AIAA Paper 2004-0559.

[19] W. Z. Strang, R. F. Tomaro, and M. J. Grismer. The defining methods of cobalt60: A paraller, implicit, unstructured euler/navier-stokes flow solver, 1999. AIAA Paper 1999-0786.

[20] P. R. Spalart and S. R. Allmaras. A one-equation turbulence model for aerodynamic flows. In *La Recherche Aerospatiale*, volume 1, pages 5–21, 1994.

[21] X. Chi, B. Zhu, T. I-P. Shih, H. E. Addy, and Y. Choo. CFD analysis of the aerodynamics of a business jet airfoil with leading-edge ice accretion, 2004. AIAA Paper 2004-0560.

[22] J. R. Forsythe, K. A. Hoffmann, and J. F. Dietiker. Detached eddy simulation of a supersonic axisymmetric base flow with an unstructured solver, 2000. AIAA Paper 2000-2410.

[23] J. Smagorinsky. General circulation experiments with the primitive equations. i. the basic experiments. *Mon. Wather Rev.*, 91:99–164, 1963.

[24] D. Thompson and B. Soni. ICEG2D: A software package for ice accretion prediction, 2003. AIAA Paper 2003-1070.

[25] M. Jiang and M. Remotigue. GUM-B grid generation code and applications. In *Numerical Grid Generation in Computational Field Simulations, Proceedings of the 6th International Conference*, London, England, July 1998.

[26] D. Marcum. *Handbook of Grid Generation, J. F. Thompson, B. K. Soni, and N. Weatherill, eds*, chapter Unstructured Grid Generation using Automatic Point Insertion and Local Reconnection. CRC Press, Boca Raton, FL, 2 edition, 1998.

[27] J. Samareh. Gridtool: A surface modeling and grid generation tool, proceedings of the workshop on surface modeling, grid generation, and related issues in CFD solutions. Technical Report NASA CP-3291, NASA, May 1995.

[28] S. Pirzadeh. Three-dimensional unstructured viscous grids by the advancing layers method. *AIAA Journal*, 34(1):43–49, January 1996.

[29] W. Z. Strang. $Cobalt_{60}$*: User's Manual*, September 2000.

[30] R. F. Tomaro, W. Z. Strang, and L. N. Sankar. An implicit algorithm for solving time dependent flows on unstructured meshes, 1997. AIAA Paper 1997-0333.

[31] http://www.faa.gov/.

[32] J. Chung and H. Addy. A numerical evaluation of icing effects on a natural laminar flow airfoil, 2000. AIAA Paper 2000-0096.

[33] D. Kenwright. Automatic detection of open and closed separation and attachment lines. In *Proceeding Visualization'98*, pages 151–158, 1998.

[34] http://www.mathworks.com/.

[35] A. Broeren. personal communication, 2004.

[36] M. B. Bragg, M. F. Kerho, and A. Khodadoust. LDV flowfield measurements on a straight and swept wing with a simulated ice accretion, 1999. AIAA Paper 1993-0300.

[37] M. B. Bragg and M. F. Kerho. LDV flowfield measurements on a 30-degree swept wing with a simulated ice accretion. Technical Report NASA CR 195327, NASA, April 1994.

REPORT DOCUMENTATION PAGE

Form Approved
OMB No. 0704-0188

Public reporting burden for this collection of information is estimated to average 1 hour per response, including the time for reviewing instructions, searching existing data sources, gathering and maintaining the data needed, and completing and reviewing the collection of information. Send comments regarding this burden estimate or any other aspect of this collection of information, including suggestions for reducing this burden, to Washington Headquarters Services, Directorate for Information Operations and Reports, 1215 Jefferson Davis Highway, Suite 1204, Arlington, VA 22202-4302, and to the Office of Management and Budget, Paperwork Reduction Project (0704-0188), Washington, DC 20503.

1. AGENCY USE ONLY (*Leave blank*)

2. REPORT DATE
November 2004

3. REPORT TYPE AND DATES COVERED
Final Contractor Report

4. TITLE AND SUBTITLE
Detached-Eddy Simulations of Separated Flow Around Wings With Ice Accretions: Year One Report

5. FUNDING NUMBERS
WBS–22–728–41–10
NAG3–2892

6. AUTHOR(S)
David Thompson and Prasad Mogili

7. PERFORMING ORGANIZATION NAME(S) AND ADDRESS(ES)
Mississippi State University
11 East Lee Boulevard
Mississippi State University, Mississippi 39762–9601

8. PERFORMING ORGANIZATION REPORT NUMBER
E–14887

9. SPONSORING/MONITORING AGENCY NAME(S) AND ADDRESS(ES)
National Aeronautics and Space Administration
Washington, DC 20546–0001

10. SPONSORING/MONITORING AGENCY REPORT NUMBER
NASA CR—2004-213379

11. SUPPLEMENTARY NOTES
Project Manager, Yung K. Choo, Propulsion Systems Division, NASA Glenn Research Center, organization code RTI, 216–433–5868.

12a. DISTRIBUTION/AVAILABILITY STATEMENT
Unclassified - Unlimited
Subject Category: 02 Distribution: Nonstandard
Available electronically at http://gltrs.grc.nasa.gov
This publication is available from the NASA Center for AeroSpace Information, 301–621–0390.

12b. DISTRIBUTION CODE

13. ABSTRACT ***(Maximum 200 words)***

A computational investigation was performed to assess the effectiveness of Detached-Eddy Simulation (DES) as a tool for predicting icing effects. The AVUS code, a public domain flow solver, was employed to compute solutions for an iced wing configuration using DES and steady Reynolds Averaged Navier-Stokes (RANS) equation methodologies. The configuration was an extruded GLC305/944-ice shape section with a rectangular planform. The model was mounted between two walls so no tip effects were considered. The numerical results were validated by comparison with experimental data for the same configuration. The time-averaged DES computations showed some improvement in lift and drag results near stall when compared to steady RANS results. However, comparisons of the flow field details did not show the level of agreement suggested by the integrated quantities. Based on our results, we believe that DES may prove useful in a limited sense to provide analysis of iced wing configurations when there is significant flow separation, e.g., near stall, where steady RANS computations are demonstrably ineffective. However, more validation is needed to determine what role DES can play as part of an overall icing effects prediction strategy. We conclude the report with an assessment of existing computational tools for application to the iced wing problem and a discussion of issues that merit further study.

14. SUBJECT TERMS
Aircraft icing; Aeronautics; Computational fluid dynamics

15. NUMBER OF PAGES
81

16. PRICE CODE

17. SECURITY CLASSIFICATION OF REPORT	18. SECURITY CLASSIFICATION OF THIS PAGE	19. SECURITY CLASSIFICATION OF ABSTRACT	20. LIMITATION OF ABSTRACT
Unclassified	Unclassified	Unclassified	